

See discussions, stats, and author profiles for this publication at: <https://www.researchgate.net/publication/260240540>

# Rate Coefficients of the $\text{Cl} + \text{CH}_3\text{C}(\text{O})\text{OCH}_3 \rightarrow \text{HCl} + \text{CH}_3\text{C}(\text{O})\text{OCH}_2$ Reaction at Different Temperatures Calculated by Transition-State Theory with ab Initio and Density Functional Theory...

ARTICLE in THE JOURNAL OF PHYSICAL CHEMISTRY A · FEBRUARY 2014

Impact Factor: 2.69 · DOI: 10.1021/jp5000864 · Source: PubMed

CITATIONS

8

READS

55

5 AUTHORS, INCLUDING:



Maggie Ng

InQpharm Group

6 PUBLICATIONS 17 CITATIONS

SEE PROFILE



Daniel K W Mok

The Hong Kong Polytechnic University

106 PUBLICATIONS 1,217 CITATIONS

SEE PROFILE



John M Dyke

University of Southampton

325 PUBLICATIONS 4,704 CITATIONS

SEE PROFILE

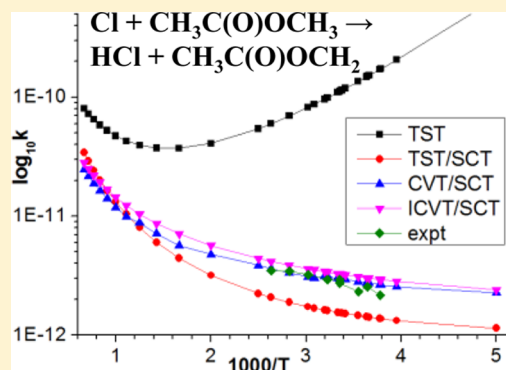
# Rate Coefficients of the $\text{Cl} + \text{CH}_3\text{C}(\text{O})\text{OCH}_3 \rightarrow \text{HCl} + \text{CH}_3\text{C}(\text{O})\text{OCH}_2$ Reaction at Different Temperatures Calculated by Transition-State Theory with *ab Initio* and Density Functional Theory Reaction Paths

Ronald Chow,<sup>†</sup> Maggie Ng,<sup>†</sup> Daniel K. W. Mok,<sup>†</sup> Edmond P. F. Lee,<sup>\*,†,‡</sup> and John M. Dyke<sup>\*,‡</sup>

<sup>†</sup>Department of Applied Biology and Chemical Technology, Hong Kong Polytechnic University, Hung Hom, Hong Kong

<sup>‡</sup>School of Chemistry, Faculty of Natural and Environmental Sciences, University of Southampton, Highfield, Southampton SO17 1BJ, United Kingdom

**ABSTRACT:** The complex relationship of computed rate coefficients ( $k$ 's) with different *ab initio*/DFT and TST levels was studied. The MEPs, gradients, and Hessians of the title reaction were computed using the MP2 and DFT methods. Electronic energies were improved to the UCCSD(T)-F12x/CBS level, and  $k$ 's were calculated at the TST, CVT, and ICVT levels with various tunnelling corrections. Although computed microcanonical and tunnelling effects are small, computed  $k^{\text{TST}}$  values are larger than computed  $k^{\text{TST/ZCT}}$  and  $k^{\text{TST/SCT}}$  values by 3 orders of magnitude at low temperatures, because computed  $\kappa^{\text{(TST/CAG)}}$  values are as small as  $6 \times 10^{-4}$ . In some cases, the maximum of the  $\Delta G^\ddagger$  curves at a certain  $T$  is far away from the MEP maximum. This raises the question of the range of  $s$  to be considered in a VTST calculation and, of a possible scenario, where no maximum on the  $\Delta G$  curve can be located and hence a breakdown of VTST occurs. For dual-level direct dynamics calculations, different entropic contributions from different lower levels can lead to computed  $k$ 's, which differ by more than 1 order of magnitude. Matching computed and experimental  $k$  values leads to an empirical barrier of 1.34 kcal mol<sup>-1</sup> for the title reaction.



## INTRODUCTION

Recently, we have reported an in-depth computational study on the reaction  $\text{H} + \text{CF}_3\text{CHFCF}_3 \rightarrow \text{H}_2 + \text{CF}_3\text{CFCF}_3$ .<sup>1</sup> This first investigation forms part of a wider project, which has the aim of ultimately establishing a consistent, reliable, and practical methodology for calculating reaction rate coefficients ( $k$ 's) in an *ab initio* manner. In ref 1, we calculated minimum energy paths (MEPs or VMEPs) of the reaction at eleven *ab initio*/density functional theory (DFT) levels, which were used to compute  $k$ 's at different temperatures ( $T$ 's) employing ten levels of transition-state theory (TST). The complex interrelationship of computed  $k$ 's with different *ab initio*/DFT and TST levels was investigated. Specifically, the effects of computed barrier heights and imaginary vibrational frequencies on computed tunnelling contributions and  $k$ 's were examined. It was concluded that computing reaction rate coefficients in an *ab initio* manner is far from straightforward or simple (see ref 1 for details). The present article is a continuation of this project. The  $\text{Cl} + \text{CH}_3\text{C}(\text{O})\text{OCH}_3$  reaction studied in this work has a lower reaction barrier than the  $\text{H} + \text{CF}_3\text{CHFCF}_3$  reaction studied in our initial work of ref 1. It offers the opportunity therefore to investigate further the effects of various levels of variational TST (VTST) on computed  $k$ 's and their relationship with different computed *ab initio*/DFT MEPs.

The title reaction,  $\text{Cl} + \text{CH}_3\text{C}(\text{O})\text{OCH}_3 \rightarrow \text{HCl} + \text{CH}_3\text{C}(\text{O})\text{OCH}_2$ , has been selected in the present study for the following reasons. First, a large number of experimental

studies on the kinetics of the  $\text{Cl} + \text{CH}_3\text{C}(\text{O})\text{OCH}_3$  reaction have been reported,<sup>2–8</sup> and it is well established from product yield analyses that the major reaction channel is H abstraction by Cl occurring almost exclusively at the methoxy ( $\text{CH}_3\text{O}$ ) end (>95%).<sup>3,4,6,8</sup> In this connection, only this reaction channel needs to be considered. Measured  $k$ 's at the temperature ( $T$ ) of 298 K obtained from these kinetic studies have values ranging from  $1.93 \pm 0.27$  to  $2.86 \pm 0.35 \times 10^{-12}$  cm<sup>3</sup> molecule<sup>-1</sup> s<sup>-1</sup> (these lower and upper limits are from refs 6 and 2, respectively; note that the value of  $7.0 \times 10^{-13}$  cm<sup>3</sup> molecule<sup>-1</sup> s<sup>-1</sup> quoted in ref 9, which was supposed to be from ref 3, is most likely a misquote). In addition to 298 K values,  $k$ 's in the  $T$  range 264.5–380 K were also measured and used to derive an Arrhenius expression,  $k = (9.31 \pm 1.02) \times 10^{-12} \exp[-(359 \pm 70)/T]$  cm<sup>3</sup> molecule<sup>-1</sup> s<sup>-1</sup>, in ref 5. However, to our knowledge, no theoretical study has been carried out on the thermodynamics and kinetics of this reaction. Second, much attention has been paid to the kinetics of this reaction by experimentalists as described above, because both the methyl acetate molecule and chlorine atom are important species in the atmosphere. Specifically, esters, with methyl acetate as a member, are an important class of oxygenated volatile organic compounds (VOCs), which are released into the atmosphere

Received: January 4, 2014

Revised: February 13, 2014

Published: February 17, 2014



**Table 1.** Some Computed Geometrical Parameters (Å), Imaginary Vibrational Frequencies ( $\omega_i$ ,  $\text{cm}^{-1}$ ) and Relative Electronic Energies ( $\Delta E_e^\ddagger$  with Respect to Separate Reactants,  $\text{kcal mol}^{-1}$ ) of the Transition State (TS) of the Reaction  $\text{Cl} + \text{CH}_3\text{C}(\text{O})\text{OCH}_3 \rightarrow \text{HCl} + \text{CH}_3\text{C}(\text{O})\text{OCH}_2$  Obtained at Different Levels of Calculations

methods <sup>a</sup>	Cl...H	H...C	$\omega_i$	$\Delta E_e^\ddagger$
UMP2	1.516	1.289	1062i	6.58
PUMP2				4.31
BH&HLYP (hybrid GGA; 50% HF exchange)	1.495	1.353	1077i	5.95
M06-2X (meta hybrid GGA; 54% HF exchange)	1.486	1.372	823i	1.83
M06 (meta hybrid GGA; 27% HF exchange)	1.500	1.366	1017i	0.43
M05 (meta hybrid GGA; 28% HF exchange)	1.540	1.306	942i	−0.47
B3LYP (hybrid GGA; 20% HF exchange)	1.460	1.446	642i	−0.49
RMP2/VDZ-F12//MP2				2.02
RMP2-F12/VDZ-F12//MP2				−0.38
RHF-UCCSD-F12a/VDZ-F12//MP2				5.31
RHF-UCCSD-F12b/VDZ-F12//MP2				5.47
RHF-UCCSD(T)-F12a/VDZ-F12//MP2				1.56
RHF-UCCSD(T)-F12b/VDZ-F12//MP2				1.72
RHF-UCCSD(T)-F12a/VDZ-F12//B3LYP				1.08
RHF-UCCSD(T)-F12b/VDZ-F12//B3LYP				1.22
RMP2/VTZ-F12//MP2				0.26
RMP2-F12/VTZ-F12//MP2				−0.24
RHF-UCCSD-F12a/VTZ-F12//MP2				6.07
RHF-UCCSD-F12b/VTZ-F12//MP2				6.08
RHF-UCCSD(T)-F12a/VTZ-F12//MP2				2.38
RHF-UCCSD(T)-F12b/VTZ-F12//MP2				2.40
RHF-UCCSD(T)-F12a/VTZ-F12//B3LYP				1.84
RHF-UCCSD(T)-F12b/VTZ-F12//B3LYP				1.84
UCCSD(T)-F12a/CBS(VDZ-F12;VTZ-F12) <sup>b</sup> //MP2				2.73
UCCSD(T)-F12b/CBS(VDZ-F12;VTZ-F12) <sup>b</sup> //MP2				2.68
UCCSD(T)-F12a/CBS(VDZ-F12;VTZ-F12) <sup>b</sup> //B3LYP				2.16
UCCSD(T)-F12b/CBS(VDZ-F12;VTZ-F12) <sup>b</sup> //B3LYP				2.11
best $\Delta E_e$ {average of UCCSD(T)-F12a,-F12b/CBS//MP2} <sup>c</sup>				2.70(31)
best $\Delta E_{0K}$ (best $\Delta E_e$ + MP2 $\Delta ZPE$ ) <sup>d</sup>				−1.44(72)
best $\Delta E_e$ + spin-orbit lowering in Cl				3.54
best $\Delta E_{0K}$ + spin-orbit lowering in Cl				−0.60

<sup>a</sup>All MP2 and DFT calculations have employed the 6-311++G\*\* basis set. The F12x//MP2 calculations were carried out by employing MP2 geometries for all species involved, whereas F12x//B3LYP indicates that the B3LYP geometry of TS was used (all other species at MP2 geometries). The spin-orbit contributions for the  $^2\text{P}$  state of Cl have not been included in the evaluation of  $\Delta E_e^\ddagger$  given in this table. The relative energies given are with the  $^2\text{P}$  state of Cl (directly from ab initio/DFT calculations, using symmetry where appropriate; see also footnote a of Table 2). <sup>b</sup>The  $1/X^3$  extrapolation formula was used for CBS extrapolation (see text). <sup>c</sup>The best estimates are averages of the CBS-F12a and CBS-F12b values. The estimated uncertainties (in parentheses) are the differences between the best and F12b/VTZ-F12 values. <sup>d</sup>Without SO contributions from Cl; computed MP2 vibrational frequencies were used for zero-point energy corrections ( $\Delta ZPE$ ) and 10% of  $\Delta ZPE$  was added to the uncertainties.

naturally from vegetation, as industrial solvents, e.g., in the manufacture of perfumes and flavoring, and as combustion products, e.g., from incomplete combustion of biodiesel (see refs 3 and 5–7, and references therein). The chlorine atom is a key atmospheric oxidant,<sup>10</sup> which can be produced via photolysis of chlorine-containing species generated in sea salt aerosols,<sup>11</sup> and surface reactions of gaseous hydrogen chloride and nitrogen oxides followed by photolysis of ClNO and ClNO<sub>2</sub>.<sup>12</sup> Also, rate coefficients for reactions of VOCs with Cl atoms are generally 10–100 times larger than those of the corresponding OH reactions,<sup>13</sup> and in the marine boundary layer (MBL), peak concentrations of Cl atoms have been measured to be in the  $10^3$ – $10^6$  atoms  $\text{cm}^{-3}$  region, giving [Cl]:[OH] ratios  $10^3$  higher than usual. All these considerations suggest that oxidation reactions of VOCs by Cl atoms are very important particularly in the MBL,<sup>14,15</sup> and reliable rate coefficients of the title reaction will be required for accurate modeling of the atmosphere. Third, during the preparation of the present manuscript, two studies on H abstraction reactions by Cl atoms were published, showing very recent interest in this

class of reactions. The first study assessed computational methodologies (ab initio/DFT and VTST) to be employed to calculate  $k$ 's for a selection of twelve H abstraction reactions from some hydrocarbons and substituted hydrocarbons by Cl.<sup>16</sup> The second study assessed structure–reactivity correlations developed for estimating gas-phase  $k$ 's for a large number of Cl + HCR<sub>3</sub>  $\rightarrow$  HCl + CR<sub>3</sub> reactions.<sup>9</sup> While both studies show the importance of this class of H abstraction reactions in many areas of chemistry (see refs 9 and 16, and references therein), the work of ref 16 is particularly relevant to the present study, as will be discussed later. Last but not least, the title reaction has a very low energy barrier ( $0.71 \pm 0.14$   $\text{kcal mol}^{-1}$  based on the exponential term of the Arrhenius expression from ref 5 given above; vide infra), which could lead to some subtle effects in the calculation of rate coefficients, as will be discussed (see also ref 16).

**Table 2.** Computed Relative Energies ( $\Delta E_0 = \Delta E_e + \Delta ZPE$ ; kcal mol<sup>-1</sup>) of the Reactant Complex (RC), Transition State (TS;  $\Delta E^\ddagger$ ), Product Complex (PC), and Separate Products ( $\Delta E^{RX}$ ), with Respect to the Separate Reactants, of the Cl + CH<sub>3</sub>C(O)OCH<sub>3</sub> → HCl + CH<sub>3</sub>C(O)OCH<sub>2</sub> Reaction Obtained at Different Levels, Used in the Calculations of Rate Coefficients

methods <sup>a</sup>	RC		$\Delta E^\ddagger$		PC		$\Delta E^{RX}$		
	$\Delta E_e$	$\Delta E_0$	$\Delta E_e$	$\Delta E_0$	$\Delta E_e$	$\Delta E_0$	$\Delta E_e$	$\Delta E_0$	$\Delta H_{298}^{RX}$
UMP2	-2.88	-2.48	7.42	3.28	0.69	-2.96	4.86	0.12	0.68
BH&HLYP	-2.43	-2.11	6.79	2.35	2.17	-1.72	4.35	-1.02	-0.30
M06-2X	-4.77	-4.35	2.67	-1.85	-3.11	-7.00	3.12	-2.05	-1.35
M06	-5.92	-5.65	1.27	-3.20	-2.68	-6.05	1.81	-3.45	-2.62
M05	-4.91	-4.50	0.37	-3.86	-3.58	-7.02	-0.05	-5.09	-4.44
B3LYP	-4.10	-3.70	0.35	-3.97	-1.25	-4.77	1.37	-3.90	-3.64
best $\Delta E_e$ (no SO) <sup>b</sup>	-3.44	-3.03	2.70	-1.44	-2.65	-6.31	0.34(30)	-4.40(77)	3.85(77)
best $\Delta E_e$ (with SO) <sup>b</sup>	-2.60	-2.19	3.54	-0.60	-1.81	-5.46	1.18	-3.56	
best $\Delta H_{298K}^b$		-2.22		-1.17		-4.96			-3.01(77)
using $\Delta H_f$ values <sup>c</sup>									-2.70, -3.19
fitted (present) <sup>d</sup>			1.34	-2.80					
experimental <sup>e</sup>			0.71						

<sup>a</sup>All MP2 and DFT calculations have employed the 6-311++G\*\* basis set. The UMP2 and DFT relative energies are from calculations with no symmetry constraint, and the  $\Delta E_e$  and  $\Delta E_0$  values given are with respect to the <sup>2</sup>P<sub>3/2</sub> spin-orbit (SO) state of Cl (including the SO contribution of 0.84 kcal mol<sup>-1</sup> lowering from the unperturbed <sup>2</sup>P state to the <sup>2</sup>P<sub>3/2</sub> SO state of Cl, unless otherwise stated; see also footnote b). <sup>b</sup>The best  $\Delta E_e$  values are the average of the UCCSD(T)-F12a/CBS//MP2 and UCCSD(T)-F12b/CBS//MP2  $\Delta E_e$  values (see footnote c of Table 1 and text), with respect to either the <sup>2</sup>P (no SO) or <sup>2</sup>P<sub>3/2</sub> (with SO) state of Cl. The best  $\Delta E_0$  and  $\Delta H_{298K}$  values were the best  $\Delta E_e$  values with  $\Delta ZPE$  and/or vibrational thermal contributions, using computed MP2 harmonic vibrational frequencies. See also footnotes c and d of Table 1. <sup>c</sup>Using available  $\Delta H_{f,298K}^\ominus$  values for the reactants and products (see text). <sup>d</sup>Best match between experimental and computed  $k$ 's (see text and Figure 11) with a fitted barrier of  $\Delta E_e^\ddagger = 0.5$  or 1.34 kcal mol<sup>-1</sup> (without and with SO correction, respectively). <sup>e</sup>From the exponential term of the Arrhenius expression from ref 5.

## ■ THEORETICAL CONSIDERATIONS AND COMPUTATIONAL DETAILS

**Ab Initio and DFT.** The general theoretical strategy, which follows that of ref 1 and has been discussed therein, will not be repeated here. In brief, geometry optimization, transition-state (TS) search, intrinsic reaction coordinate (IRC; a GAUSSIAN input keyword) path (or minimum energy path, VMEP, in POLYRATE notation), and harmonic vibrational frequency calculations were carried out using the GAUSSIAN09 suite of programs<sup>17</sup> at the MP2, B3LYP, BH&HLYP, M05, M06, and M06-2X levels with the 6-311++G\*\* basis set. The functionals chosen are hybrid (B3LYP and BH&HLYP) and meta hybrid (M05, M06, and M06-2X) GGA functionals, with various amounts of Hartree–Fock (HF) exchange (from 20 to 54%; Table 1). The computed reaction barriers ( $\Delta E_e^\ddagger$ ) of the title reaction using these functionals and including values (UMP2 and PUMP2) obtained from MP2 calculations range from -0.49 to +6.58 kcal mol<sup>-1</sup> (without including spin-orbit contributions from the <sup>2</sup>P state of Cl; Tables 1 and 2, and later text). The computed harmonic frequencies of the imaginary vibrational mode of the TS have values between 642i and 1077i cm<sup>-1</sup> (Table 1). These selected single-level methods (as used for single-level dynamics, cf. dual-level dynamics, calculations of  $k$ ; vide infra) provide a reasonable range of theoretical variables (e.g., the amounts of HF exchange, the magnitudes of the computed barrier heights and imaginary vibrational frequencies of the TS) for an in-depth analysis of the interrelationship of various theoretical levels employed to calculate  $k$ 's.

Improved relative electronic energies, which were subsequently used in dual-level dynamics calculations of  $k$  (vide infra), were computed in the present study using the explicit correlation methods, UCCSD(T)-F12x ( $x = a$  or  $b$ ),<sup>18</sup> as implemented in the MOLPRO suite of programs<sup>19,20</sup> instead of the RCCSD(T) method used in ref 1. These explicit correlation methods provide a dramatic improvement of basis set

convergence when compared with conventional correlation methods {e.g., CCSD(T)}.<sup>21</sup> Basis sets specifically designed for F12 calculations, namely, the cc-pVXZ-F12 and cc-pVXZ-F12\_OPTRI,  $X = D$  or  $T$ , basis sets<sup>22,23</sup> for the atomic orbital (AO) and resolution of the identity (RI) basis sets, respectively, were used in these F12 calculations, together with the corresponding aug-cc-pVXZ\_MP2FIT basis sets<sup>24</sup> for the density fitting (DF) basis sets. The scaled perturbative triples obtained by a simple scaling factor,  $\Delta E(T_{sc}) = \Delta E(T) \times E_{corr}^{MP2-F12}/E_{corr}^{MP2}$  (i.e., the ratio between the computed correlation energies obtained at the RMP2 and RMP2-F12 levels)<sup>25</sup> have been employed in all UCCSD(T)-F12x calculations throughout. With the triple- $\zeta$  (TZ) quality basis sets, the AO, RI, and DF basis sets for the reaction system considered consist of 435, 696, and 953 contracted Gaussian functions, respectively. Computed T1 diagnostics for all species considered have values <0.018, indicating negligible multi-reference character in the computed CCSD wave functions. In addition, the  $1/X^3$  extrapolation formula<sup>26,27</sup> was used to obtain computed UCCSD(T)-F12x relative electronic energies at the complete basis set (CBS) limit. The averages of the computed UCCSD(T)-F12a/CBS//MP2/6-311++G\*\* and UCCSD(T)-F12b/CBS//MP2/6-311++G\*\* relative electronic energies are taken as the best theoretical estimates of computed relative electronic energies (vide infra).

We have also computed the torsional barriers of the two methyl groups in CH<sub>3</sub>C(O)OCH<sub>3</sub>, and the methyl torsional barrier in CH<sub>3</sub>C(O)OCH<sub>2</sub> at various levels of calculation, as described above. For the TS, the methyl torsional barrier was estimated by rotating the methyl group by 60° from the first order saddle point without further optimization.

**TST Calculations of  $k$ 's.** Computed IRC paths obtained at different ab initio and/or DFT levels by GAUSSIAN09 were employed to calculate extrapolated/interpolated VMEPs in both single- and dual-level direct dynamics calculations of  $k$ 's



using POLYRATE version 2010-A.<sup>28</sup> Specifically, for all single levels, 15 IRC points on each side of the TS with a step size of 0.1 amu<sup>1/2</sup> bohr (the unit used by GAUSSIAN09) were requested, and associated gradients and Hessians (using the Calcall keyword in GAUSSIAN09) were computed analytically for all IRC points. For the MP2, BH&HLYP, M05, and M06 IRC calculations, 31 points in total, including the TS, on each IRC path were computed, and the ranges of the reaction coordinate (*s*) cover at least the range  $-1.56 \leq s \leq 1.56$  amu<sup>1/2</sup> bohr (with *s* = 0 for the TS). However, the IRC calculations with the B3LYP and M06-2X functionals stopped at the thirteenth and ninth points, respectively, from the TS in the direction toward the reactants (i.e., negative *s*), where a minimum was reached in each case with the default optimization thresholds used in the IRC calculations. The corresponding *s* values at these points, where the IRC calculations stopped, are  $-1.4717$  and  $-0.8763$  amu<sup>1/2</sup> bohr, and the optimized structures are clearly those of the separate reactants of Cl and CH<sub>3</sub>C(O)OCH<sub>3</sub> (in the  $-OCH_3$  group for the H to be removed, C $\cdots$ H = 1.161 and 1.178 Å at the B3LYP and M06-2X levels respectively), though the two separate reactants are still quite close to each other (H $\cdots$ Cl = 1.818 and 1.725 Å), when compared to the corresponding optimized structures of the reactant complex (H $\cdots$ Cl = 2.986 and 2.996 Å), suggesting very flat computed B3LYP and M06-2X energy surfaces in this region. It is very likely that similar situations occur in ref 16 for some H abstraction reactions by Cl (when it is noted that some IRC paths are not sufficiently extensive for the maxima on the IRCmax, ZK-IRCmax, and VTST reaction paths to be reached, in footnote b of their Table 2). Nevertheless, in the direction toward the products from the TS (i.e., positive *s*), 15 IRC points were computed with *s* values reaching 1.8266 and 1.6442 amu<sup>1/2</sup> bohr at the B3LYP and M06-2X levels, respectively. It should also be noted that in the B3LYP and M06-2X IRC calculations, some IRC points took large numbers of steps to achieve convergence in the optimization procedure. Using the Hessian based predictor-corrector (HPC) reaction path following method<sup>29</sup> in the IRC calculation of GAUSSIAN09, with the keyword, Calcall, the Hessian is computed analytically only once after the first predictor step for each IRC point, because the corrected end point and predicted end point are expected to lie within the same quadratic region of the energy surface within the theory of the HPC method.<sup>30</sup> However, in some cases, where the IRC points take large numbers of steps to converge, when the vibrational frequencies, obtained using the Hessian computed after the first predictor step, are plotted against *s*, the resulting frequency versus *s* curves could be bumpy at these IRC points, because the optimized geometry of the final IRC point differs significantly from the initial geometry. In these cases, extra vibrational frequency calculations were carried out at the converged geometries of the IRC points. The computed Hessians from these single-geometry frequency calculations were then used in the inputs for these IRC points in the calculation of *k*'s using POLYRATE. The resulting curves of vibrational frequency versus *s* are then found to be smooth.

In direct dynamics calculations of *k*'s using POLYRATE, the step size used in the reaction coordinates for interpolation/extrapolation of the VMEP is SSTEP = 0.0002 amu<sup>1/2</sup> Å (the unit used in POLYRATE; the default SSTEP value is 0.000265 amu<sup>1/2</sup> Å) in all cases. The ranges of *s* considered for interpolation/extrapolation of the VMEP curve {also the *V*<sub>a</sub>*G* (=VMEP + ΔZPE) and free energy (Δ*G*) curves; vide infra}

are, however, case dependent. It is because the maxima of the computed free energy (Δ*G* versus *s*) curves at certain *T*'s can, in some cases, be quite far away from the TS at *s* = 0 amu<sup>1/2</sup> bohr. This will be discussed in detail in the next section. It just needs to be emphasized here that care was taken to ensure that the *s* ranges considered in the present investigation cover the maxima of all computed Δ*G* curves. This is particularly important for the  $-s$  side of the reaction (i.e., in the direction toward the reactants), as the maximum of a Δ*G* curve at a certain *T* can have an *s*<sup>\*</sup>(Δ*G*) value as negative as  $-2.8$  amu<sup>1/2</sup> Å (the \* notation is used to denote generally the maximum of a curve in the present article). It has been found that, when the *s* range is inadequate to cover *s*<sup>\*</sup>(Δ*G*), the search of the maximum on the Δ*G* curve in a VTST calculation stops at an *s* value with the largest Δ*G* value within the *s* range used, which is not the true maximum, because the *s* range used does not cover the maximum. Consequently, with an inadequate *s* range, the computed VTST *k* would be erroneously large, as the largest Δ*G* value used to calculate *k* is smaller than the true maximum Δ*G* value.

Ten levels of TST in total, namely, conventional TST, canonical variational TST (CVT), and interpolated CVT (ICVT), and with the semiclassical tunneling correction of Wigner<sup>31</sup> (W), the zero-curvature (ZCT), and small-curvature (SCT) tunneling corrections,<sup>32</sup> namely, TST/W, TST/ZCT, CVT/ZCT, ICVT/ZCT, TST/SCT, CVT/SCT, and ICVT/SCT, have been considered as previously in ref 1. The symmetry factor used in the rate coefficient calculation is unity. It should also be noted that, in all *k* calculations, both the <sup>2</sup>P<sub>3/2</sub> and <sup>2</sup>P<sub>1/2</sub> spin-orbit states of Cl were considered {i.e., using the correct electronic partition functions, in terms of the degeneracies, and with an energy separation of 882.35 cm<sup>-1</sup> (=0.0040 hartree; as estimated from the experimental spin-orbit splitting<sup>33</sup>) between the two spin-orbit states}. Spin-orbit contributions lower the energy of the unperturbed <sup>2</sup>P state of Cl by ~0.84 kcal mol<sup>-1</sup> to the <sup>2</sup>P<sub>3/2</sub> state. In addition, all methyl torsional modes have been treated within the hindered-internal-rotator (hir) approximation employing the full Chuang-Truhlar (CT) method.<sup>34,35</sup> With the RO (an input keyword in POLYRATE, referring to the *R* $\omega$  scheme in ref 34, where the reduced moment of inertia of the rotator is calculated in rectilinear coordinates and the torsional partition function is calculated with the specified torsional mode in normal-mode analysis) scheme, the torsional barrier (*W*<sub>*j*</sub>) is estimated using the equation,  $W_j = 2I_j(\omega_j/M)^2$ , where *I*<sub>*j*</sub> is the moment of inertia for internal rotation,  $\omega_j$  is the computed harmonic torsional frequency, and *M* is the total number of minima along the torsional coordinate.<sup>34</sup> We have also employed the RWO scheme, where computed torsional barriers obtained in the present study were used instead of the estimated ones by POLYRATE. Both schemes gave essentially identical computed *k*'s.

Regarding dual-level direct dynamics calculations of *k*'s, where computed relative electronic energies of the IRC path (or VMEP) obtained at a lower level are improved by higher level energy calculations at the geometries of the lower level IRC path, it was found that the higher level VMEPs obtained with the method of mapping used in POLYRATE were unrealistic in the present study, particularly for IRC paths with low barriers. Consequently, a simple method has been derived to obtain higher level energies on a lower level IRC path, which are then used instead of the lower level energies in a single-level direct dynamics calculation, to mimic the dual-level direct

dynamics method implemented in POLYRATE. The following expression was used to evaluate a higher level energy ( $E_s^{\text{HL}}$ ) to replace the lower level energy ( $E_s^{\text{LL}}$ ) at a certain  $s$  (for the reactant side of the IRC):

$$E_s^{\text{HL}} = (E_s^{\text{LL}} - E_{\text{RC}}^{\text{LL}}) \times \{(E_{\text{TS}}^{\text{HL}} - E_{\text{RC}}^{\text{HL}})/(E_{\text{TS}}^{\text{LL}} - E_{\text{RC}}^{\text{LL}})\} + E_{\text{RC}}^{\text{HL}}$$

The superscripts, HL and LL, refer to energies of the higher and lower levels, respectively. The subscripts, RC, TS, and  $s$ , refer to the reactant complex, the transition state and a point on the IRC path or VMEP at a reaction coordinate  $s$ .  $\{(E_{\text{TS}}^{\text{HL}} - E_{\text{RC}}^{\text{HL}})/(E_{\text{TS}}^{\text{LL}} - E_{\text{RC}}^{\text{LL}})\}$  is a simple scaling factor, which is the ratio between the higher level reaction barrier and the lower level reaction barrier, both with respect to the reactant complexes of the corresponding levels. A similar expression is used for the product side of the IRC path. The higher level employed in the present study is the best theoretical estimate, the averages of the UCCSD(T)-F12a/CBS and UCCSD(T)-F12b/CBS values. Only the energies at the higher level of the five stationary points on the IRC path of the lower level, namely, separate reactants and products, reactant and product complexes, and TS, are required to be computed explicitly. The higher level energies of nonstationary points on the lower level IRC path are evaluated using the above expression, and replace the lower level energies as inputs in a single-level POLYRATE calculation. All resulting higher level VMEPs with different lower level VMEPs have the same five higher level stationary points, but slightly different higher level nonstationary points on the VMEPs, as will be discussed later.

## RESULTS AND DISCUSSION

**Ab Initio/DFT Results.** Some optimized geometrical parameters and computed harmonic vibrational frequencies of the imaginary mode ( $\omega_i$ ) of the TS, and computed reaction barriers ( $\Delta E_e^\ddagger$ ) obtained at different ab initio/DFT levels are given in Table 1 (spin contamination in all open-shell doublet states considered is negligibly small, with computed  $\langle S^2 \rangle$  values in the region 0.750–0.763 for DFT and 0.750–0.786 for UMP2). First, it can be seen that, although the range of the computed Cl...H values in the TS is relatively small {between 1.540 (M05) and 1.460 (B3LYP) Å; a spread of 0.08 Å}, that of H...C is quite large {between 1.446 (B3LYP) and 1.289 (UMP2) Å; a spread of 0.157 Å}. It may be concluded that, because the UMP2 H...C bond length is the shortest, the UMP2 method gives a more reactant like TS structure than those obtained with the different functionals used. However, the M05 H...C bond length of 1.306 Å is only 0.017 Å larger than the UMP2 value. In any case, no obvious trend can be deduced from these computed geometrical parameters obtained at different levels of calculation. This shows the well-known lack of systematic correlation with DFT, for example, in this case, in terms of the amount of exact exchange in the functional (Table 1; some similar observations are discussed below). Second, computed  $\omega_i$  values range from 642i (B3LYP) to 1077i (BH&HLYP)  $\text{cm}^{-1}$ . The spread of over 460i  $\text{cm}^{-1}$  is quite large. However, again, no obvious trend can be found in these computed values. Third, the computed  $\Delta E_e^\ddagger$  values obtained from single-level calculations range from +6.58 (UMP2) to −0.49 (B3LYP)  $\text{kcal mol}^{-1}$ , with a spread of 7  $\text{kcal mol}^{-1}$ . It may be considered that computed  $\Delta E_e^\ddagger$  values follow roughly the amounts of exact exchange included in the methods employed to calculate them. Specifically, larger amounts of

exact exchange seem to give larger computed  $\Delta E_e^\ddagger$  values. Fourth, regarding computed higher level  $\Delta E_e^\ddagger$  values obtained from F12 calculations {namely, RMP2, RMP2-F12, UCCSD-F12x, and UCCSD(T)-F12x, where  $x = a$  or  $b$ }, it can be seen that contributions from triple excitations are considerable ( $\sim 3.8$   $\text{kcal mol}^{-1}$ ). However, basis size effects are relatively small (differences of  $\sim 0.8$   $\text{kcal mol}^{-1}$  between using the VDZ-F12 and VTZ-F12 basis sets), as expected with the explicitly correlated F12 methods. We have also used the B3LYP geometry of the TS (the geometries of the reactants and products are very similar with different single levels; see footnote a of Table 1) in F12 calculations to assess geometry effects on computed  $\Delta E_e^\ddagger$  values. Using the B3LYP geometry instead of the MP2 geometry for the TS gives slightly lower computed UCCSD(T)-F12x barrier heights (by ca. 0.5  $\text{kcal mol}^{-1}$ ), indicating that geometry effects on the computed relative electronic energies are not negligible, but acceptably small, despite the MP2 and B3LYP TS structures (e.g., the computed H...C bond lengths discussed above) being quite different. This also suggests that the region of the UCCSD(T)-F12x energy surface near the saddle point is flat. In addition, it should be noted that the differences in the computed  $\Delta ZPE$ s and thermal vibrational energies obtained between employing the computed B3LYP and MP2 harmonic vibrational frequencies are quite small ( $< 0.20$   $\text{kcal mol}^{-1}$  for  $\Delta E_0^\ddagger$  and/or  $\Delta H_{298\text{K}}^\ddagger$  and  $< 0.54$   $\text{kcal mol}^{-1}$  for  $\Delta E_0^{\text{RX}}$  and/or  $\Delta H_{298\text{K}}^{\text{RX}}$ ). Lastly, the best computed  $\Delta E_e^\ddagger$  and  $\Delta E_0^\ddagger$  (at the ab initio UCCSD(T)-F12/CBS//MP2/6-311++G\*\* level; see footnote d of Table 1) obtained in the present study, without SO contributions to Cl, are  $+2.70 \pm 0.31$  and  $-1.44 \pm 0.72$   $\text{kcal mol}^{-1}$  ( $+3.54$  and  $-0.60$   $\text{kcal mol}^{-1}$  including SO contributions to Cl; see also Table 2), respectively. If the best  $\Delta E_e^\ddagger$  value given in Table 1 is considered as the benchmark, among all the DFT values, the computed M06-2X  $\Delta E_e^\ddagger$  value of 1.83  $\text{kcal mol}^{-1}$  (2.67  $\text{kcal mol}^{-1}$  including SO contributions to Cl) agrees best with the benchmark value (a difference of 0.87  $\text{kcal mol}^{-1}$ ). The rest differ from the benchmark by more than 2  $\text{kcal mol}^{-1}$ .

Table 2 gives computed relative energies ( $\Delta E_e$ ,  $\Delta E_0$ , and  $\Delta H_{298\text{K}}$ ) of the reactant complex (RC), TS ( $\Delta E^\ddagger$ ), product complex (PC), and separate products ( $\Delta E^{\text{RX}}$ ), with respect to the separate reactants, of the  $\text{Cl} + \text{CH}_3\text{C}(\text{O})\text{OCH}_3 \rightarrow \text{HCl} + \text{CH}_3\text{C}(\text{O})\text{OCH}_2$  reaction, obtained at different levels of calculation. These values were used in the calculations of  $k$ 's by POLYRATE. It should be noted that, for the single levels, the energies used for all species involved in rate coefficient calculations were computed without any symmetry constraint, for all species to be aligned on the reaction surface (values given in Table 1 were computed with appropriate symmetry constraints). However, for the computationally more demanding F12 calculations, symmetry was used, whenever possible, to save computing time. In addition, the values given in Table 2 are relative to the  $^2P_{3/2}$  spin-orbit state of Cl (i.e., the spin-orbit contributions from the  $^2P$  state of Cl have been included), unless otherwise stated (footnote a of Table 2). From Table 2, the spreads of the computed relative energies of the RC and the PC are 3.49 and 5.75  $\text{kcal mol}^{-1}$ , respectively, relative to the reactants. No obvious trends can be observed from these values. The best  $\Delta E_e$  values or the benchmarks for the RC and PC relative energies are  $-2.60$  and  $-1.81$   $\text{kcal mol}^{-1}$ , respectively. For the RC, the UMP2 and BH&HLYP values of  $-2.88$  and  $-2.43$   $\text{kcal mol}^{-1}$  agree very well with the benchmark (differences of only  $-0.28$  and  $+0.17$   $\text{kcal mol}^{-1}$ ). For the

Table 3. Computed Methyl Torsional Barrier Heights ( $\Delta E_e$ , kcal mol<sup>-1</sup>) Obtained at Different Levels of Calculations

methods	CH <sub>3</sub> C(O)OCH <sub>3</sub> <sup>a</sup>		TS <sup>b</sup>	CH <sub>3</sub> C(O)OCH <sub>2</sub> <sup>a</sup>
	CH <sub>3</sub> -O	CH <sub>3</sub> -C	CH <sub>3</sub> -C	CH <sub>3</sub> -C
B3LYP/6-11++G**	0.811	0.174	0.639	0.211
BH&HLYP/6-311++G**	1.015	0.313		0.389
M05/6-311++G**	0.681	0.141		0.162
M06/6-311++G**	0.919	0.217		0.246
M06-2X/6-311++G**	1.237	0.313		0.392
MP2/6-311++G**	1.437	0.223	0.897	0.223
RMP2/VDZ-F12//MP2	1.174	0.232	0.912	0.336
RMP2-F12/VDZ-F12//MP2	1.168	0.200	0.872	0.301
UCCSD-F12a/VDZ-F12//MP2	1.218	0.310	0.958	0.395
UCCSD-F12b/VDZ-F12//MP2	1.231	0.320	0.967	0.402
UCCSD(T)-F12a/VDZ-F12//MP2	1.134	0.233	0.890	0.318
UCCSD(T)-F12b/VDZ-F12//MP2	1.146	0.243	0.879	0.325
RMP2/VDZ-F12//B3LYP <sup>c</sup>	1.234	0.327	0.195	0.444
RMP2-F12/VDZ-F12//B3LYP	1.244	0.336	0.199	0.417
UCCSD-F12a/VDZ-F12//B3LYP	1.167	0.306	0.187	0.420
UCCSD-F12b/VDZ-F12//B3LYP	1.199	0.334	0.188	0.420
UCCSD(T)-F12a/VDZ-F12//B3LYP	1.187	0.337	0.190	0.426
UCCSD(T)-F12b/VDZ-F12//B3LYP	1.193	0.341	0.190	0.426
RMP2/VTZ-F12//MP2	1.188	0.207	0.875	0.307
RMP2-F12/VTZ-F12//MP2	1.162	0.197	0.864	0.296
UCCSD-F12a/VTZ-F12//MP2	1.206	0.307	0.950	0.391
UCCSD-F12b/VTZ-F12//MP2	1.212	0.312	0.955	0.394
UCCSD(T)-F12a/VTZ-F12//MP2	1.127	0.237	0.887	0.319
UCCSD(T)-F12b/VTZ-F12//MP2	1.132	0.241	0.891	0.323
RMP2/VTZ-F12//B3LYP	1.266	0.340	0.197	0.424
RMP2-F12/VTZ-F12//B3LYP	1.227	0.322	0.199	0.397
UCCSD-F12a/VTZ-F12//B3LYP	1.139	0.284	0.188	0.398
UCCSD-F12b/VTZ-F12//B3LYP	1.142	0.286	0.188	0.409
UCCSD(T)-F12a/VTZ-F12//B3LYP	1.161	0.320	0.192	0.409
UCCSD(T)-F12b/VTZ-F12//B3LYP	1.164	0.322	0.191	0.410
UCCSD(T)-F12a/CBS(1/X <sup>3</sup> )/MP2	1.124	0.238	0.886	0.320
UCCSD(T)-F12b/CBS(1/X <sup>3</sup> )/MP2	1.126	0.241	0.896	0.323
UCCSD(T)-F12a/CBS(1/X <sup>3</sup> )/B3LYP	1.150	0.313	0.193	0.403
UCCSD(T)-F12b/CBS(1/X <sup>3</sup> )/B3LYP	1.151	0.314	0.193	0.403
average of all CBS values	1.14(2)	0.28(4)	0.54(35)	0.36(4)
CCSD(T)/cc-pVTZ <sup>d</sup>	1.18	0.28		
experimental <sup>e</sup>	1.21	0.29		

<sup>a</sup>The relevant methyl group was rotated by 60° from the true minimum, followed by full geometry optimization of the rest of the geometrical parameters. The optimized structures have only one a" imaginary mode, which is that of the methyl torsional mode at all levels, except for CH<sub>3</sub>COOCH<sub>2</sub> at the BH&HLYP, M06-2X and MP2 levels, where the optimized structures have two a" imaginary modes corresponding to the CH<sub>2</sub>-O and CH<sub>3</sub>-C torsions. <sup>b</sup>The methyl group was rotated by 60° from the true minimum, without further optimization. <sup>c</sup>The structures at the torsional barriers were from B3LYP calculations, whereas those at the minima were from MP2 (same for all labels with B3LYP below). <sup>d</sup>Computed vibrationally corrected barriers (413.1 and 99.2 cm<sup>-1</sup>) from ref 44. <sup>e</sup>422 and 102 cm<sup>-1</sup>; derived from a fit to microwave and millimeter wave transitions of *cis*-methyl acetate (ref 45).

PC, the B3LYP value of -1.25 kcal mol<sup>-1</sup> is larger than the benchmark by 0.56 kcal mol<sup>-1</sup>, whereas the M06 value of -2.68 kcal mol<sup>-1</sup> is smaller than the benchmark by 0.87 kcal mol<sup>-1</sup>.

Computed  $\Delta E_e^\ddagger$  values have been discussed above and will not be repeated here. It is just noted that the theoretical benchmark for the barrier height of +3.54 ( $\Delta E_e^\ddagger$ ) or -0.60 ( $\Delta E_0^\ddagger$ , including  $\Delta ZPE$ ) kcal mol<sup>-1</sup> obtained in the present study may be compared with the experimentally derived activation energy of  $0.71 \pm 0.14$  kcal mol<sup>-1</sup> obtained from the Arrhenius expression of ref 5. However, it has been noted previously in ref 1 that a reaction barrier height is not a directly measurable quantity. The raw experimental data, which are used to derive a barrier height, are measured *k*'s at different *T*'s. Different theoretical approaches can be used (e.g., employing

different forms of the modified Arrhenius equation<sup>36-39</sup>) to derive a barrier height from measured *k*'s, and they give different "experimentally derived" barrier heights. In this connection, a direct comparison between computed and experimentally derived barrier heights may not be meaningful. When theoretical and experimental kinetics values are compared, it is more appropriate to compare computed and measured *k*'s (vide infra) than to compare computed and experimentally derived barrier heights.

Computed  $\Delta E_e^{\text{RX}}$  values have a spread of 4.9 kcal mol<sup>-1</sup>. The computed benchmark value is 1.18 kcal mol<sup>-1</sup> (Table 2). The B3LYP value of 1.37 kcal mol<sup>-1</sup> agrees best with the benchmark value, followed by the M06 value of 1.81 kcal mol<sup>-1</sup>. However, when computed  $\Delta H_{298\text{K}}^{\text{RX}}$  values are considered, the bench-



mark of  $-3.01 \text{ kcal mol}^{-1}$  is between the B3LYP value ( $-3.64 \text{ kcal mol}^{-1}$ ) and the M06 value ( $-2.62 \text{ kcal mol}^{-1}$ ). These comparisons show that zero-point energy corrections ( $\Delta ZPE$ ) and thermal vibrational contributions (evaluated using computed harmonic vibrational frequencies) to  $\Delta H_{298K}^{RX}$ , obtained with different functionals, can be quite different. The effects of  $\Delta ZPE$  and entropic contributions on computed  $k$ 's will be discussed later. The enthalpies of formation ( $\Delta H_{f,298K}^\ominus$ ) of the reactants and products of the reaction considered are available:<sup>40</sup>  $\text{HCl} = -22.060 \pm 0.024 \text{ kcal mol}^{-1}$  and  $\text{Cl} = 28.992 \pm 0.002 \text{ kcal mol}^{-1}$ , both from CODATA,<sup>41</sup>  $\text{CH}_3\text{C}(\text{O})\text{OCH}_3 = -98.0 \text{ kcal mol}^{-1}$  from rotating bomb calorimetry,<sup>42</sup> and  $\text{CH}_3\text{C}(\text{O})\text{OCH}_2 = -49.65 \pm 0.14 \text{ kcal mol}^{-1}$  from MC-QCISD//MP2/6-311G\*\* calculations.<sup>43</sup> Reference 43 also gives a computed MC-QCISD  $\Delta H_{f,298K}^\ominus$  value for  $\text{CH}_3\text{C}(\text{O})\text{OCH}_3$  ( $-97.51 \pm 0.33 \text{ kcal mol}^{-1}$ ), which differs from the only available experimental value of ref 42 by  $\sim 0.5 \text{ kcal mol}^{-1}$ . This comparison between theory and experiment suggests uncertainties of  $\sim 0.5 \text{ kcal mol}^{-1}$  associated with the available  $\Delta H_{f,298K}^\ominus$  values of  $\text{CH}_3\text{C}(\text{O})\text{OCH}_3$  and  $\text{CH}_3\text{C}(\text{O})\text{OCH}_2$ . Employing the above available  $\Delta H_{f,298K}^\ominus$  values to evaluate the reaction enthalpy,  $\Delta H_{298K}^{RX}$  values of  $-2.70$  {using the experimental  $\Delta H_{f,298K}^\ominus$  value for  $\text{CH}_3\text{C}(\text{O})\text{OCH}_3$ } and  $-3.19$  {using the MC-QCISD  $\Delta H_{f,298K}^\ominus$  value for  $\text{CH}_3\text{C}(\text{O})\text{OCH}_3$ }  $\text{kcal mol}^{-1}$  are obtained. These values agree very well (within  $0.3 \text{ kcal mol}^{-1}$ ) with the theoretical benchmark  $\Delta H_{298K}^{RX}$  value of  $-3.01 \text{ kcal mol}^{-1}$  obtained in the present study (Table 2).

Computed methyl torsional barriers of various species involved in the reaction considered, obtained at different levels of calculation, are summarized in Table 3. For  $\text{CH}_3\text{C}(\text{O})\text{OCH}_3$  and  $\text{CH}_3\text{C}(\text{O})\text{OCH}_2$ , the best computed methyl torsional barriers for  $\text{CH}_3\text{-C}$  are  $0.28$  and  $0.36 (\pm 0.04) \text{ kcal mol}^{-1}$ , respectively, suggesting essentially free internal rotations (as  $k_b T$  at  $300 \text{ K} = 0.59 \text{ kcal mol}^{-1}$ ). The best computed  $\text{CH}_3\text{-O}$  torsional barrier in  $\text{CH}_3\text{C}(\text{O})\text{OCH}_3$  is  $1.12 \pm 0.02 \text{ kcal mol}^{-1}$ , suggesting a hindered internal rotation. With the TS, because the geometries used to calculate the methyl torsional barrier height have not been optimized, the computed values are expected to be upper limits. In addition, the differences in the computed methyl torsional barrier heights obtained between B3LYP and MP2 geometries of the TS are not small (generally  $\sim 0.8 \text{ kcal mol}^{-1}$ ), indicating that geometry effects on computed barrier heights of the TS are not negligible. Computed methyl torsional barrier heights of the TS as shown in Table 3 have values between  $\sim 0.2$  and  $\sim 1.0 \text{ kcal mol}^{-1}$ . The average of all computed UCCSD(T)-F12x/CBS values is  $0.54 \pm 0.35 \text{ kcal mol}^{-1}$ , suggesting a nearly free internal rotation. For  $\text{CH}_3\text{C}(\text{O})\text{OCH}_3$ , recently reported CCSD(T)/cc-pVTZ torsional barriers<sup>44</sup> for  $\text{CH}_3\text{-O}$  and  $\text{CH}_3\text{-C}$  are  $1.18$  and  $0.28 \text{ kcal mol}^{-1}$ , and available experimentally derived values<sup>45</sup> are  $1.21$  and  $0.29 \text{ kcal mol}^{-1}$ , respectively. Summing up, all the methyl torsional barrier values considered are very consistent with each other, indicating reasonable reliability.

**Rate Coefficient Calculations: VMEP,  $\Delta ZPE$ , and  $V_a G$  of Single Levels.** First, computed IRC, VMEP,  $\Delta ZPE$ , and  $V_a G$  ( $=\text{VMEP} + \Delta ZPE$ ) curves obtained at six single levels are considered and they are shown in Figure 1. The IRC points (black squares in Figure 1) are from GAUSSIAN09 calculations, whereas the VMEP,  $\Delta ZPE$ , and  $V_a G$  curves are from POLYRATE interpolation/extrapolation. The energies of all the curves shown in Figure 1 are with respect to separate reactants (set to zero at  $s = -\infty$ ). Because the RC, which is

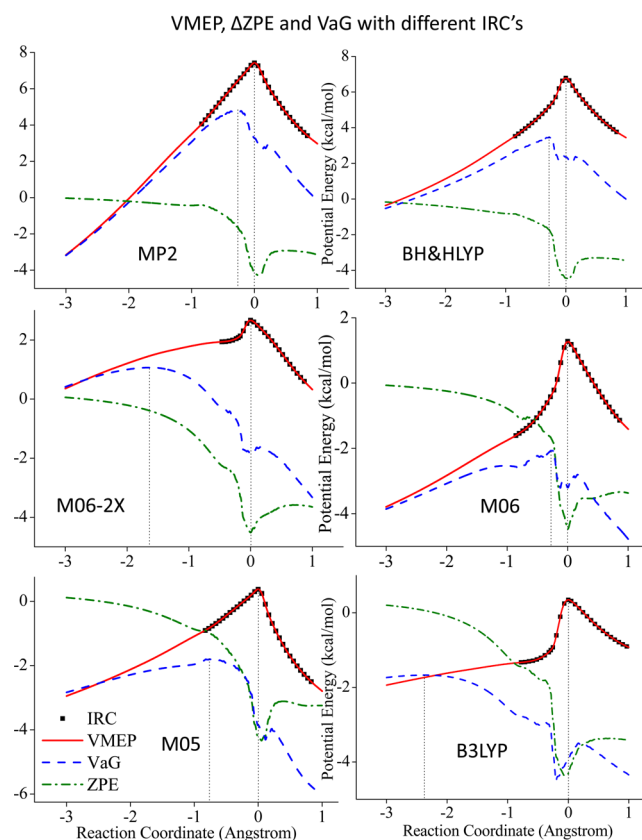


**Figure 1.** IRC (black squares; from G09 calculations), VMEP,  $\Delta ZPE$ , and  $V_a G$  (from POLYRATE interpolation/extrapolation) curves at six single levels. Energies in  $\text{kcal mol}^{-1}$  are with respect to separate reactants, which are set to zero; see text.

lower in energy than the separate reactants in all cases (Table 2), is included in the rate coefficient calculations, the VMEP and  $V_a G$  curves shown in Figure 1 move to lower energies toward the RC ( $-s$  values). However, each  $\Delta ZPE$  curve shown in Figure 1 has a dip near the TS (i.e., around  $s = 0$ ). While the imaginary vibrational mode and two low frequency intermolecular modes in the TS correlate with three translational modes in the separate reactants and products, a CH stretching mode with computed harmonic frequencies of  $\sim 3100 \text{ cm}^{-1}$  in the reactant,  $\text{CH}_3\text{C}(\text{O})\text{OCH}_3$ , and the HCl stretching mode with computed harmonic frequencies of  $\sim 3000 \text{ cm}^{-1}$  in the product, HCl, correlate with an asymmetric intermolecular  $\text{C}\cdots\text{H}\cdots\text{Cl}$  mode in the TS with computed harmonic frequencies in the  $\sim 500 \text{ cm}^{-1}$  region {computed values between  $459$  (M05) and  $553$  (B3LYP)  $\text{cm}^{-1}$ }. The dips in all the  $\Delta ZPE$  curves shown in Figure 1 are mainly due to gradual changes along the reaction paths of the computed harmonic vibrational frequencies from the CH stretching mode at the methyl group of the reactant, where H abstraction takes place, toward the  $\text{C}\cdots\text{H}\cdots\text{Cl}$  intermolecular mode in the TS, and then to the HCl stretching mode in HCl. The dips of  $\sim 4 \text{ kcal mol}^{-1}$  in all the  $\Delta ZPE$  curves near the TS at  $s = 0$ , as shown in Figure 1, are mainly due to half of the differences between the above-mentioned computed CH and  $\text{C}\cdots\text{H}\cdots\text{Cl}$  frequencies ( $\sim 1300 \text{ cm}^{-1}$  or  $\sim 3.7 \text{ kcal mol}^{-1}$ ). However, it should be noted that, although the minima of all  $\Delta ZPE$  curves are near  $s = 0$ , they are not necessarily, in all cases, exactly at  $s = 0$ , where the maxima of all corresponding VMEP curves are. Consequently, the dips in the  $V_a G$  curves, resulting from the dips of the  $\Delta ZPE$  curves,



**Table 4.** Some Single-Level Results<sup>a</sup> Employing Different IRCs (Energies in kcal mol<sup>-1</sup> and Rate Coefficients in cm<sup>3</sup> molecule<sup>-1</sup> s<sup>-1</sup>; See Text)

	B3LYP	M05	M06	M06-2X	BH&HLYP	UMP2
$\Delta E_e^\ddagger$	0.35	0.37	1.27	2.67	6.70	7.42
$\Delta E_0^\ddagger$	-3.97	-3.86	-3.20	-1.85	2.35	3.28
$s^*(V_aG)$	-2.37	-0.76	-0.28	-1.64	-0.28	-0.27
$\Delta V_aG$	-2.30	-2.05	-1.13	-2.92	-1.12	-1.54
$k^{CVT} = k^{ICVT}$	yes	yes	yes	yes	yes	yes
$\kappa^{ZCT} \approx \kappa^{SCT} \approx 1.0$	yes	yes	yes	yes	$T \geq 750$ K	$T \geq 750$ K
$\kappa^{TST/CAG,200K}$	$3.09 \times 10^{-3}$	$5.75 \times 10^{-3}$	$5.88 \times 10^{-2}$	$6.50 \times 10^{-4}$	$6.00 \times 10^{-2}$	$2.09 \times 10^{-2}$
$\kappa^{CVT/CAG,200K}$	$9.99 \times 10^{-1}$	$9.88 \times 10^{-1}$	1.00	$9.96 \times 10^{-1}$	1.00	$9.99 \times 10^{-1}$
$k^{TST,200K}$	$1.65 \times 10^{-8}$	$1.00 \times 10^{-8}$	$3.13 \times 10^{-9}$	$1.07 \times 10^{-10}$	$2.30 \times 10^{-15}$	$1.54 \times 10^{-16}$
$k^{TST/CAG,200K}$	$5.10 \times 10^{-11}$	$5.76 \times 10^{-11}$	$1.84 \times 10^{-10}$	$6.98 \times 10^{-14}$	$1.38 \times 10^{-16}$	$3.22 \times 10^{-18}$
$k^{CVT,200K}$	$3.85 \times 10^{-11}$	$1.05 \times 10^{-10}$	$1.71 \times 10^{-10}$	$4.66 \times 10^{-14}$	$2.02 \times 10^{-16}$	$4.58 \times 10^{-18}$
$k^{ICVT/SCT,200K}$	$3.85 \times 10^{-11}$	$1.05 \times 10^{-10}$	$1.71 \times 10^{-10}$	$4.80 \times 10^{-14}$	$4.51 \times 10^{-16}$	$1.02 \times 10^{-17}$
$\kappa^{TST/CAG,1500K}$	$4.63 \times 10^{-1}$	$5.03 \times 10^{-1}$	$6.85 \times 10^{-1}$	$3.76 \times 10^{-1}$	$6.87 \times 10^{-1}$	$5.97 \times 10^{-1}$
$\kappa^{CVT/CAG,1500K}$	$9.81 \times 10^{-1}$	$7.25 \times 10^{-1}$	$9.97 \times 10^{-1}$	$9.29 \times 10^{-1}$	1.00	$9.87 \times 10^{-1}$
$k^{TST,1500K}$	$1.49 \times 10^{-10}$	$1.25 \times 10^{-10}$	$1.18 \times 10^{-10}$	$8.40 \times 10^{-11}$	$1.63 \times 10^{-11}$	$1.04 \times 10^{-11}$
$k^{TST/CAG,1500K}$	$6.88 \times 10^{-11}$	$6.27 \times 10^{-11}$	$8.07 \times 10^{-11}$	$3.16 \times 10^{-11}$	$1.12 \times 10^{-11}$	$6.23 \times 10^{-12}$
$k^{CVT,1500K}$	$1.98 \times 10^{-11}$	$3.36 \times 10^{-11}$	$3.06 \times 10^{-11}$	$7.67 \times 10^{-12}$	$7.48 \times 10^{-12}$	$4.37 \times 10^{-12}$
$k^{ICVT/SCT,1500K}$	$1.98 \times 10^{-11}$	$3.36 \times 10^{-11}$	$3.06 \times 10^{-11}$	$7.67 \times 10^{-12}$	$7.60 \times 10^{-12}$	$4.43 \times 10^{-12}$
$s^*(\Delta G)^{200K}$	-2.34	-0.54	-0.27	-1.69	-0.27	-0.27
$s^*(\Delta G)^{1500K}$	-1.94	-2.88	-0.27	-2.34	-0.27	-0.23
$\omega_i/\text{cm}^{-1}$	642i	942i	1017i	823i	1077i	1062i
$T/K$ with $\kappa^{TST/W} \leq 1.2$	$\geq \sim 500$	$\geq \sim 650$	$\geq \sim 700$	$\geq \sim 600$	$\geq \sim 750$	$\geq \sim 700$

<sup>a</sup>Computed activation energies,  $\Delta E_e^\ddagger$  (electronic energy differences at  $s = 0$ , including spin-orbit contribution for CI), and  $\Delta V_aG$  values ( $V_aG = \text{VMEP} + \text{ZPE}$ ;  $\Delta V_aG$  is the difference between the  $V_aG$  energy at  $s = 0$  and the maximum of  $V_aG$  at  $s^*(V_aG)$ ) are in kcal mol<sup>-1</sup> {negative for  $V_aG(s=0)$  smaller than  $V_aG(s^*)$ }. Computed rate coefficients,  $k$ 's, are in cm<sup>3</sup> molecule<sup>-1</sup> s<sup>-1</sup>. Reaction coordinate,  $s$ , is in amu<sup>1/2</sup> Å. The maximum of VMEP is at  $s = 0$ , the maximum of  $V_aG$  is at  $s^*(V_aG)$ , and the maximum of  $\Delta G$  at a certain temperature,  $T$ , is at  $s^*(\Delta G)^{TK}$ . The computed imaginary harmonic vibrational frequency,  $\omega_i$ , at the TS ( $s = 0$ ) is in cm<sup>-1</sup>.

may be slightly bumpy and/or not exactly at  $s = 0$ . Also, the shapes of the  $\Delta ZPE$  and VMEP curves are quite different. Consequently, the resulting  $V_aG$  curves of six single theoretical levels used, shown in Figure 1, are quite different. In any case, the following features in the  $V_aG$  curves should be noted. First, in general, a dip with two maxima on either side can be seen in each  $V_aG$  curve shown in Figure 1. However, in the cases of MP2 and BH&HLYP, the dips in the  $V_aG$  curves are less prominent than in the corresponding  $\Delta ZPE$  curves, because relatively high barriers are seen in the VMEP curves (with the  $\Delta E_e^\ddagger$  values of 7.42 and 6.79 kcal mol<sup>-1</sup> respectively; Table 2). The dips in the  $V_aG$  curves become more obvious in cases with relatively low VMEP barriers. Second, the dips of the  $V_aG$  curves are generally near  $s = 0$ , as the minimum of the  $\Delta ZPE$  curves are all near  $s = 0$ , as mentioned above. Third, the maximum of the  $V_aG$  curve at the  $-s$  side of the dip is always higher in energy than that at the  $+s$  side. This is mainly because the PC is generally lower in energy ( $V_aG$ ) than the RC (in all cases with the only exception of BH&HLYP; see  $\Delta E_0$  values of RC and PC in Table 2) and/or because the regions of all  $\Delta ZPE$  curves in the  $+s$  side are always lower in energy than those in the  $-s$  side (Figure 1). Last but not least, the positions of the global maxima of the  $V_aG$  curves,  $s^*(V_aG)$ , are marked by dotted lines in Figure 1 and their values given in Table 4. It can be seen from Figure 1 and Table 4 that, although  $s^*(V_aG)$  is always in the  $-s$  side, its value or position depends not only on the corresponding VMEP barrier height but also on the detailed differences between the shapes of the VMEP and  $\Delta ZPE$  curves near the TS, particularly when the VMEP barrier is low.

The first obvious effect of  $s^*(V_aG)$  being different from  $s = 0$  is on the classical transmission coefficient for correcting the

classical threshold of conventional TST,  $\kappa^{TST/CAG}$  (the classical adiabatic ground-state correction, CAG), which accounts for the fact that the conventional TS (at  $s = 0$ , the maximum of the VMEP curve) is not at the maximum of the vibrationally adiabatic ground-state potential curve,  $s^*(V_aG)$ .<sup>46</sup> Generally, a computed  $k$  at the TST or CVT level including a multidimensional tunnelling correction (MT; e.g., ZCT or SCT) is expressed as<sup>32</sup>

$$k(\text{with tunnelling}) = \kappa^{CAG} \times \kappa(\text{tunnelling}) \times k(\text{without tunnelling})$$

i.e.,

$$k^{(TST \text{ or } CVT)/MT} = \kappa^{(TST \text{ or } CVT)/CAG} \times \kappa^{MT} \times k^{(TST \text{ or } CVT)}$$

When MT is included at the TST or CVT level,  $\kappa^{TST/CAG}$  or  $\kappa^{CVT/CAG}$  is also included (considered as a part of tunnelling correction). At the TST level,  $\kappa^{TST/CAG} = \exp\{\beta[V_aG(s=0) - V_aG(s^*)]\}$ , where  $\beta = 1/RT$  (see refs 32 and 46). Generally, because  $V_aG(s^*) \geq V_aG(s=0)$ ,  $\kappa^{TST/CAG}$  is always  $\leq 1$  (see also ref 1). The differences between  $V_aG(s^*)$  and  $V_aG(s=0)$  for all six single levels are given in Table 4 { $\Delta V_aG$  is the difference between the  $V_aG$  values at  $s^*(V_aG)$  and  $s = 0$ }, together with the corresponding  $s^*(V_aG)$  values. Also, the corresponding  $\kappa^{TST/CAG}$ ,  $k^{TST}$ , and  $k^{TST/CAG}$  values at 200 and 1500 K are given in Table 4. The range of  $\Delta V_aG$  values with six single levels is -2.92 to -1.12 kcal mol<sup>-1</sup> (with the M06-2X and BH&HLYP  $V_aG$ 's, respectively; Table 4), whereas the corresponding ranges of computed  $\kappa^{TST/CAG}$  values at 200 and 1500 K are  $6.50 \times 10^{-4}$  to  $6.00 \times 10^{-2}$  and  $3.76 \times 10^{-1}$  to  $6.87 \times 10^{-1}$ , respectively. In any case, the correlations among computed  $\Delta V_aG$ ,  $\kappa^{TST/CAG}$ ,

$k^{\text{TST}}$ , and  $k^{\text{TST/CAG}}$  values given in Table 4 are clear, as they just follow the expressions for  $\kappa^{\text{TST/CAG}}$  and  $k^{(\text{TST or CVT})/\text{CAG}}$  given above (for  $\kappa^{\text{CVT/CAG}}$ , see later text). In summary, the most outstanding observations are the large effects of  $\kappa^{\text{TST/CAG}}$  (as small as  $6.5 \times 10^{-4}$ ) on computed  $k^{\text{TST/CAG}}$  values, especially at low  $T$ 's, causing the  $k^{\text{TST/CAG}}$  values to be more than 3 orders of magnitude smaller than the corresponding  $k^{\text{TST}}$  values (e.g., with the M06-2X  $V_{\text{a}}G$  at 200 K). These dramatic effects of  $\kappa^{\text{TST/CAG}}$  on computed  $k^{\text{TST/CAG}}$  values originate from  $\Delta ZPE$  changes along the VMEP, which is mainly due to the change of the CH stretching mode in the reactant,  $\text{CH}_3\text{C}(\text{O})\text{OCH}_3$ , to the intermolecular  $\text{C}\cdots\text{H}\cdots\text{Cl}$  mode in the TS.

At the CVT level,  $\kappa^{\text{CVT/CAG}}$  values at 200 and 1500 K are tabulated in Table 4. They have values of almost exactly 1.0 at 200 K and near 1.0 at 1500 K for all cases, with the only exception of the M05  $\kappa^{\text{CVT/CAG,1500K}}$  value of  $7.25 \times 10^{-1}$ , which may be considered as not far from 1.0. At the CVT level, the generalized transition state (GTS) is at the maximum of the  $\Delta G$  curve,  $s^*(\Delta G)$ , and hence  $\kappa^{\text{CVT/CAG}} = \exp\{\beta(V_{\text{a}}G(s^*(\Delta G)) - V_{\text{a}}G(s^*))\}$ .<sup>32,46</sup> When the  $V_{\text{a}}G$  values at  $s^*(V_{\text{a}}G)$  and  $s^*(\Delta G)$  are almost identical, the corresponding  $\kappa^{\text{CVT/CAG}}$  values are near 1.0. In these cases, the  $\Delta G$  curves are generally behaving as the corresponding  $\Delta V_{\text{a}}G$  curves, and the GTS at the CVT level is near the maximum of the  $V_{\text{a}}G$  curve, i.e.,  $s^*(\Delta G) \approx s^*(V_{\text{a}}G)$ . However, although  $s^*(\Delta G)^{200\text{K}}$  and  $s^*(\Delta G)^{1500\text{K}}$  values (i.e., the reaction coordinates of the maximum in the  $\Delta G$  versus  $s$  curves at a certain  $T$ ) given in Table 4 are generally close to the corresponding  $s^*(V_{\text{a}}G)$  values, there are exceptions, such as the M05, M06-2X, and B3LYP  $s^*(\Delta G)^{1500\text{K}}$  values of  $-2.88$ ,  $-2.34$ , and  $-1.94$  amu<sup>1/2</sup> Å, which differ from the corresponding  $s^*(V_{\text{a}}G)$  values of  $-0.76$ ,  $-1.64$ , and  $-2.37$  amu<sup>1/2</sup> Å by  $-2.12$ ,  $+0.70$ , and  $+0.43$  amu<sup>1/2</sup> Å, respectively. Nevertheless, apart from M05, which will be discussed later, the above comparisons indicate that the maxima of the  $\Delta G$  curves at 200 and 1500 K are close to the corresponding maxima of the  $V_{\text{a}}G$  curves for most cases. In the cases with the M06-2X and B3LYP VMEPs, although their  $s^*(V_{\text{a}}G)$  values differ from the corresponding  $s^*(\Delta G)^{1500\text{K}}$  as mentioned above, because both the  $\Delta G$  and  $V_{\text{a}}G$  curves are quite flat near their maxima (vide infra), their  $\kappa^{\text{CVT/CAG}}$  values are still near 1.0. In summary, because  $\Delta G$  and  $\Delta V_{\text{a}}G$  curves behave in a similar way,  $\kappa^{\text{CVT/CAG}}$  values are close to unity. In this connection, variational effects at the CVT level are actually similar to the CAG corrections at the TST level, and CAG corrections at the TST level move computed  $k^{\text{TST/CAG}}$  values close to the corresponding computed  $k^{\text{CVT}}$  values.

Before considering the M05 case, where  $s^*(\Delta G)^{1500\text{K}}$  differs significantly from  $s^*(V_{\text{a}}G)$ , we consider variations of  $s^*(\Delta G)$  with  $T$  for all six single levels in Figure 2. It can be seen that all the  $s^*(\Delta G)$  curves have smooth changes with  $T$ , with the only exception of the M05 case, where there are sudden changes at 400/500 and 900/1000 K and then  $s^*(\Delta G)$  decreases at higher  $T$ 's toward  $s = -3.0$  amu<sup>1/2</sup> Å (i.e., toward the RC side). With MP2, BH&HLYP, and M06 (the M06 data points in Figure 2 are almost exactly underneath those of BH&HLYP), changes in  $s^*(\Delta G)$  with  $T$  are negligibly small, and their values are very close to the corresponding  $s^*(V_{\text{a}}G)$  values (Table 4). However, although  $s^*(\Delta G)$  increases with  $T$  for B3LYP, it decreases for M06-2X. One important observation from the above considerations for the cases of B3LYP, M06-2X, and M05 (to be discussed in more detail below) is that  $s^*(\Delta G)$  can carry on, in some cases, decreasing toward the RC (more negative  $s$  values) with increasing (M06-2X and M05) or decreasing

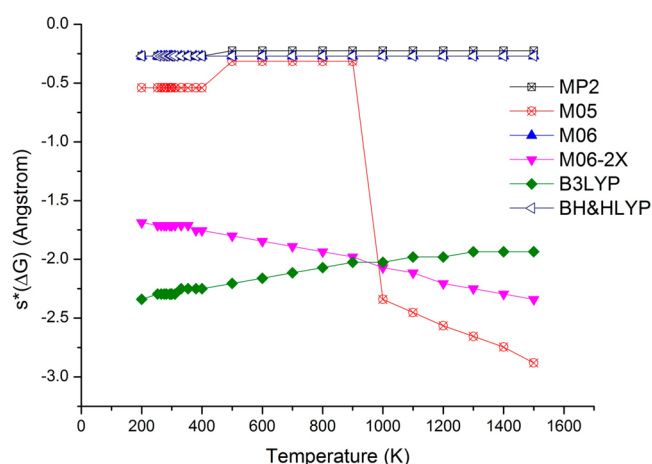


**Figure 2.** Positions (reaction coordinate,  $s$ , amu<sup>1/2</sup> Å) of the global maxima in the free energy ( $\Delta G$ ) curves,  $s^*(\Delta G)$ , versus temperature ( $T$ , K) at six single levels. Note that the BH&HLYP plot is almost exactly on top of the M06 plot.

(B3LYP)  $T$ . As mentioned above, similar situations have been encountered in ref 16 for some H abstraction reactions by Cl even at the fixed temperature of 298 K, and to locate approximate maxima on the IRCmax, ZK-IRCmax, and VTST reaction paths, the authors of ref 16 had to extend the reaction paths beyond the computed IRC paths (see footnote *b* of Table 2 in ref 16). In summary, such situations can lead to two issues. First, the range of  $s$  to be considered is case dependent and may be inadequate for certain  $T$ 's, in the sense that the  $s$  range employed may not cover  $s^*(\Delta G)$ , the maximum in the  $\Delta G$  curve. We have mentioned earlier, in the section Theoretical Consideration and Computational Details, that it is important to make sure the  $s$  range employed does cover  $s^*(\Delta G)$ . Second, in the extreme case, where  $s^*(\Delta G)$  reaches the RC at a certain  $T$ , resulting in no maximum on the  $\Delta G$  curve, the applicability of VTST, which depends on locating the maximum of the  $\Delta G$  curve, is in question. Actually, the  $\Delta G$  curve published in Figure 4 of ref 16 for the  $(\text{CH}_3)_2\text{CH}_2 + \text{Cl} \rightarrow (\text{CH}_3)_2\text{CH} + \text{HCl}$  reaction appears to increase continuously toward negative  $s$ , suggesting that this problem may be present in this case.

Coming back to the M05  $\Delta G$  versus  $s$  curves, the curves at 400/500 K and 900/1000 K are shown in Figure 3, with the position of the global maximum in each  $\Delta G$  curve indicated (with an arrow and the  $s^*$  value). It can be seen that the change in  $s^*(\Delta G)$  between 400 (bottom trace) and 500 (top trace) K is due to a slight shift of the position of the maximum on the "flat plateau" of the  $\Delta G$  curve near the TS, whereas that between 900 (bottom trace) and 1000 (top trace) K is due to a swap of the global maximum from the plateau near the TS (900 K) to another flatter plateau at more negative  $s$  (1000 K). Nevertheless, in all cases, although the changes in the  $s^*(\Delta G)$  values are not small, the changes in the corresponding  $\Delta G$  values are small, because the plateaus considered are flat and hence the corresponding  $\Delta G$  values are close in energy. It should be noted that the very flat plateau of the  $\Delta G$  curve at more negative  $s$  values in Figure 3 is likely a consequence of slightly unsmooth extrapolation of the VMEP,  $\Delta ZPE$ , and  $V_{\text{a}}G$  curves beyond the IRC points (Figure 1). If the extra dip (other than the one near  $s = 0$  due to the dip in the  $V_{\text{a}}G$  curve discussed above), which has caused the appearance of another plateau in the  $\Delta G$  curve at more negative  $s$ , is due to an artifact arising from extrapolation of the  $V_{\text{a}}G$  curve beyond the IRC

## Free Energy at M05 Level at Different Temperatures

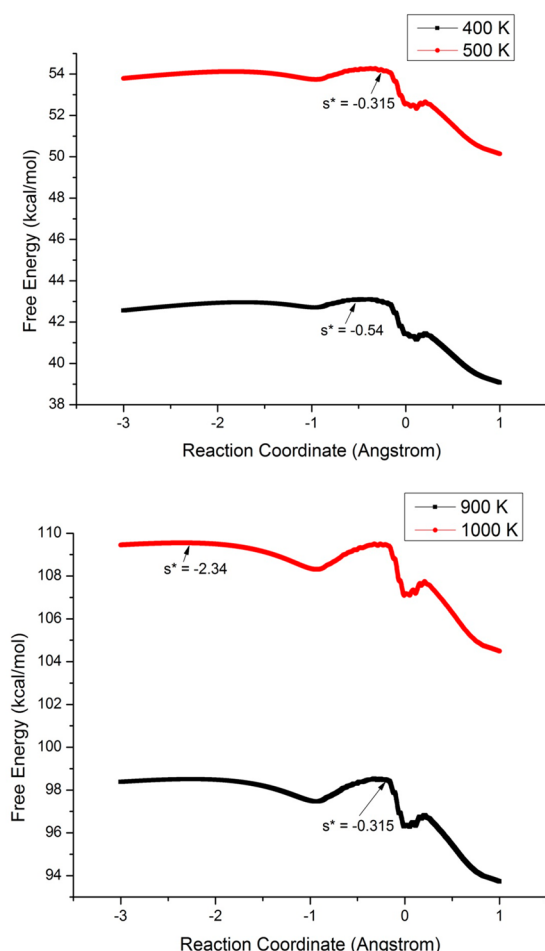


**Figure 3.** Free energy ( $\Delta G$ , kcal mol<sup>-1</sup>) versus reaction coordinate ( $s$ , amu<sup>1/2</sup> Å) plots at 400 and 500 K (top) and at 900 and 1000 K (bottom). The global maxima at four temperatures are indicated (see text).

points, then without this artifact, the  $\Delta G$  curve would be expected just to continue without the dip, and be very flat in the  $-s$  region.

**Rate Coefficient Calculations: Computed  $k$ 's at Single Levels.** Before the computed  $k$ 's obtained at the six single levels used are considered, the following points should be noted. First, at each level, the computed  $k^{\text{CVT}}$  and  $k^{\text{ICVT}}$  values are identical in all cases (Table 4), indicating negligible microcanonical effects. Second, computed  $\kappa^{\text{TST/W}}$  values, which depend only on computed imaginary vibrational frequencies ( $\omega_i$ ), have values  $\geq 1.2$  for  $T$  between  $\geq 500$  and  $\geq 750$  K (Table 4). Because it has been noted that when  $\kappa^{\text{TST/W}} > \sim 1.2$ , this correction should not be used (ref 32), Wigner tunnelling corrections will not be considered further. Third, ZCT and SCT corrections are negligible (i.e.,  $\kappa^{\text{ZCT}} = \kappa^{\text{SCT}} = \sim 1.0$ ) for all  $T$ 's considered, except with the MP2 and BH&HLYP IRC paths, where  $\kappa^{\text{SCT}}$  and  $\kappa^{\text{ZCT}} < \sim 1.5$  at 298 K, which may be considered as small. Fourth, although computed  $k^{\text{CVT}}$  and  $k^{\text{ICVT}}$  values are identical in all cases, and ZCT and SCT corrections are 1.0 in most cases, computed  $k^{\text{CVT/SCT}}$  and  $k^{\text{ICVT/SCT}}$  values may differ (Table 4), when  $\kappa^{\text{CVT/CAG}}$  is not negligible (i.e., smaller than 1.0), because the generalized transition-state (GTS) dividing surface at the ICVT level is at the maximum of

$V_a G$ , and hence there is no CAG correction with ICVT, unlike the case with CVT. Last, because some computed  $k$ 's obtained at different TST levels have the same values as discussed above, in the figures with computed  $k$  versus  $T$  curves and discussions below, only one set of these  $k$ 's with the same values were considered for the sake of simplicity.

Some representative computed  $k$  versus  $T$  plots obtained at different single levels are compared with available experimental values in Figure 4 ( $k^{\text{TST}}$ , the lowest TST level with different

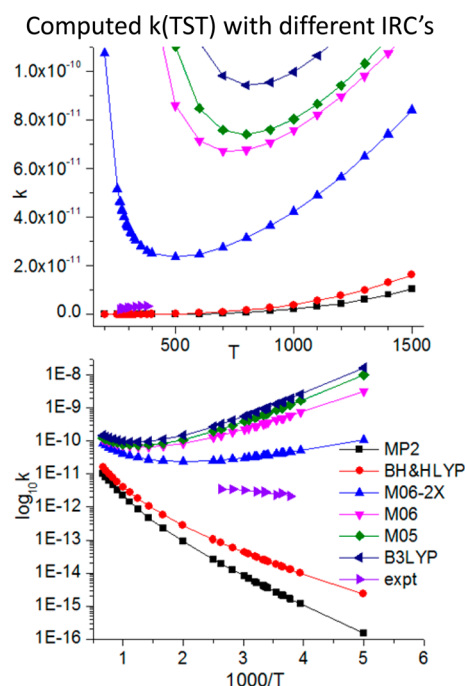


**Figure 4.** Computed  $k^{\text{TST}}$  (cm³ molecule<sup>-1</sup> s<sup>-1</sup>) versus  $T$  (K) curves (top) and  $\log_{10} k^{\text{TST}}$  versus  $1000/T$  curves (bottom) obtained with different single-level IRC paths (experimental values from ref 5).

IRC paths), Figure 5 ( $k^{\text{ICVT/SCT}}$ , the highest TST level), and Figure 6 (various TST levels with the M06-2X IRC path). Considering computed  $k^{\text{TST}}$  values in Figure 4, it is clear that their magnitudes mainly follow the computed barrier heights (i.e., a larger  $\Delta E_e^\ddagger$  gives a smaller  $k^{\text{TST}}$ ; see also Table 4), and available experimental values are between the computed BH&HLYP and M06-2X values. However, with  $k^{\text{ICVT/SCT}}$  (Figure 5), when the barrier heights are relatively low with the M06, M05, and B3LYP IRC paths, variational effects can change the order of computed  $k$ 's compared to the order at the TST level. Specifically, computed barrier heights have the order M06 > M05 > B3LYP ( $\Delta E_e^\ddagger = 1.27, 0.37$ , and  $0.35$  kcal mol<sup>-1</sup>; Table 4), and the corresponding computed  $k^{\text{TST}}$  values have magnitudes in the reverse order of  $\Delta E_e^\ddagger$ , as expected (Figure 4), but computed  $k^{\text{ICVT/SCT}}$  values have the order B3LYP > M05 > M06 (Figure 5), contrary to expectation based only on the computed barrier heights, suggesting that the effects due to the pre-exponential entropic (or partition function) term become more prominent when the barrier height is low. In any case, with the computed  $k^{\text{ICVT/SCT}}$  values, the experimental values are now between the M06-2X and B3LYP values. If only barrier heights are considered, then a barrier height between those of M06-2X and B3LYP ( $\Delta E_e^\ddagger = 0.35$  and  $2.67$  kcal mol<sup>-1</sup> respectively; Table 4) may give a better match between computed  $k^{\text{ICVT/SCT}}$  and experimental values. Figure 6 shows  $k$



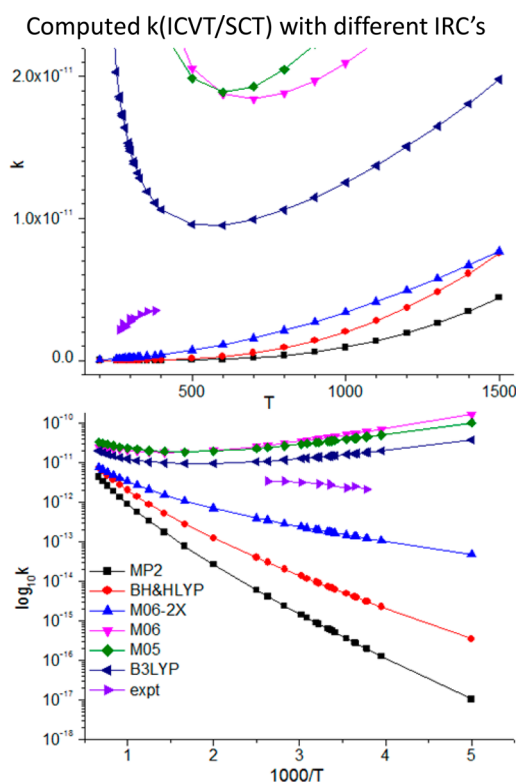


**Figure 5.** Computed  $k^{\text{ICVT/SCT}}$  ( $\text{cm}^3 \text{ molecule}^{-1} \text{ s}^{-1}$ ) versus  $T$  (K) curves (top) and  $\log_{10} k^{\text{ICVT/SCT}}$  versus  $1000/T$  curves (bottom) obtained with different single-level IRC paths (experimental values from ref 5).

versus  $T$  plots obtained at different TST levels employing the M06-2X IRC path. These plots are representative of all single levels; computed  $k^{\text{TST}}$  values are significantly larger than the  $k$ 's computed at higher TST (and/or VTST) levels, but large CAG corrections result in computed  $k^{\text{TST/CAG}}$  values being close to the  $k$ 's computed at higher levels. This is because the effects of variational effects at the CVT (and ICVT) levels are actually similar to the effects of CAG corrections at the TST level, as discussed above.

**Rate Coefficient Calculations: Computed  $k$ 's at Dual Levels.** Before computed  $k$ 's obtained at dual levels are discussed, lower (single) and higher (dual) level VMEPs employed in these dual-level calculations of  $k$ 's, shown in Figure 7, need to be considered. The dual-level VMEP's were obtained using the simple formula given above, which fixes all dual-level VMEPs to the higher level energies of the reactants, products, RC, PC, and TS. It can be seen that all higher level VMEPs with different lower levels have the same barrier height, as expected, and mimic the corresponding single-level VMEPs closely in shape. Computed  $k^{\text{TST}}$  and  $k^{\text{ICVT/SCT}}$  versus  $T$  plots obtained with the six dual-level VMEPs (i.e., the same higher level with six lower levels) are given in Figure 8 and 9, respectively. First, for both  $k^{\text{TST}}$  and  $k^{\text{ICVT/SCT}}$ , the spreads of computed values with six different lower levels are more than 1 order of magnitude. This shows the large effects from the different lower levels employed in these dual-level calculations. Different lower levels have different pre-exponential entropic terms of the free energy, which affect the computed  $k$  values. Second, the magnitudes of computed  $k^{\text{TST}}$  values with different lower levels follow the order  $\text{M06-2X} > \text{M06} > \text{BH\&HLYP} > \text{M05} > \text{MP2} > \text{B3LYP}$ , whereas those of  $k^{\text{ICVT/SCT}}$ ,  $\text{M06} >$

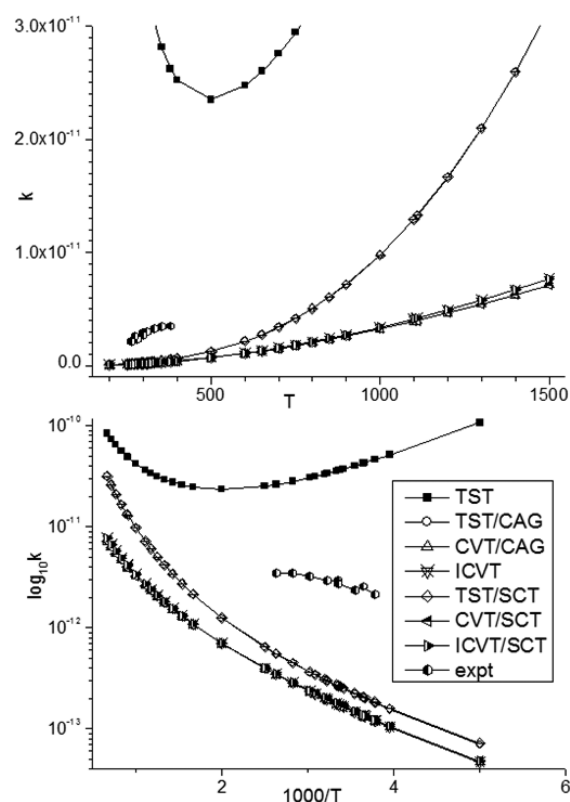


**Figure 6.** Computed  $k$  ( $\text{cm}^3 \text{ molecule}^{-1} \text{ s}^{-1}$ ) versus  $T$  (K) curves (top) and  $\log_{10} k$  versus  $1000/T$  curves (bottom) obtained at various TST levels with the M06-2X IRC path (experimental values from ref 5). Because  $k^{\text{CVT}} = k^{\text{ICVT}}$  and  $k^{\text{ZCT}} = k^{\text{SCT}}$  ( $\approx 1$ ), computed  $k$ 's with the same values are not plotted. For those plotted, the  $k^{\text{TST/CAG}}$  curve essentially overlaps with the  $k^{\text{TST/SCT}}$  curve, whereas the  $k^{\text{CVT/CAG}}$ ,  $k^{\text{ICVT}}$ ,  $k^{\text{CVT/SCT}}$ , and  $k^{\text{ICVT/SCT}}$  curves overlap with each other (see text).

$\text{BH\&HLYP} > \text{B3LYP} > \text{M05} > \text{MP2} > \text{M06-2X}$ . There is no obvious trend in these orders. Third, when compared with available experimental values, although computed  $k^{\text{TST}}$  values obtained at dual levels with the lower levels of MP2 and M05 give very good agreement, all computed  $k^{\text{ICVT/SCT}}$  values are too low by around 1 order of magnitude. On the basis of computed  $k^{\text{ICVT/SCT}}$  values at the highest TST level considered in the present study, comparison between theory and experiment suggests that the best computed F12/CBS//MP2 barrier height of  $3.54 \text{ kcal mol}^{-1}$  (Table 4) is too high. Last, computed  $k$  versus  $T$  plots obtained at different TST levels employing the MP2 lower level in the dual-level calculations are shown in Figure 10. It can be seen that computed  $k^{\text{TST}}$  values are larger than all other computed  $k$  values, similar to those with single levels (e.g., with the M06-2X IRC path; Figure 6), discussed above.

To obtain the best match between theory and experiment, empirical adjustments of the barrier height in the dual-level approach have been carried out. The following highest levels of theory have been selected for this purpose. First, only computed  $k^{\text{ICVT/SCT}}$  values are considered in the adjustment, as ICVT/SCT is the highest TST level considered. Second, regarding the higher level IRC path, the purely ab initio F12/CBS//MP2 higher level has been used, with the only exception of the barrier height, which is adjusted empirically to obtain the best match between theory and experiment. Third, regarding the choice of the lower level to be employed in the dual-level



## Single and dual level VMEP Curves)

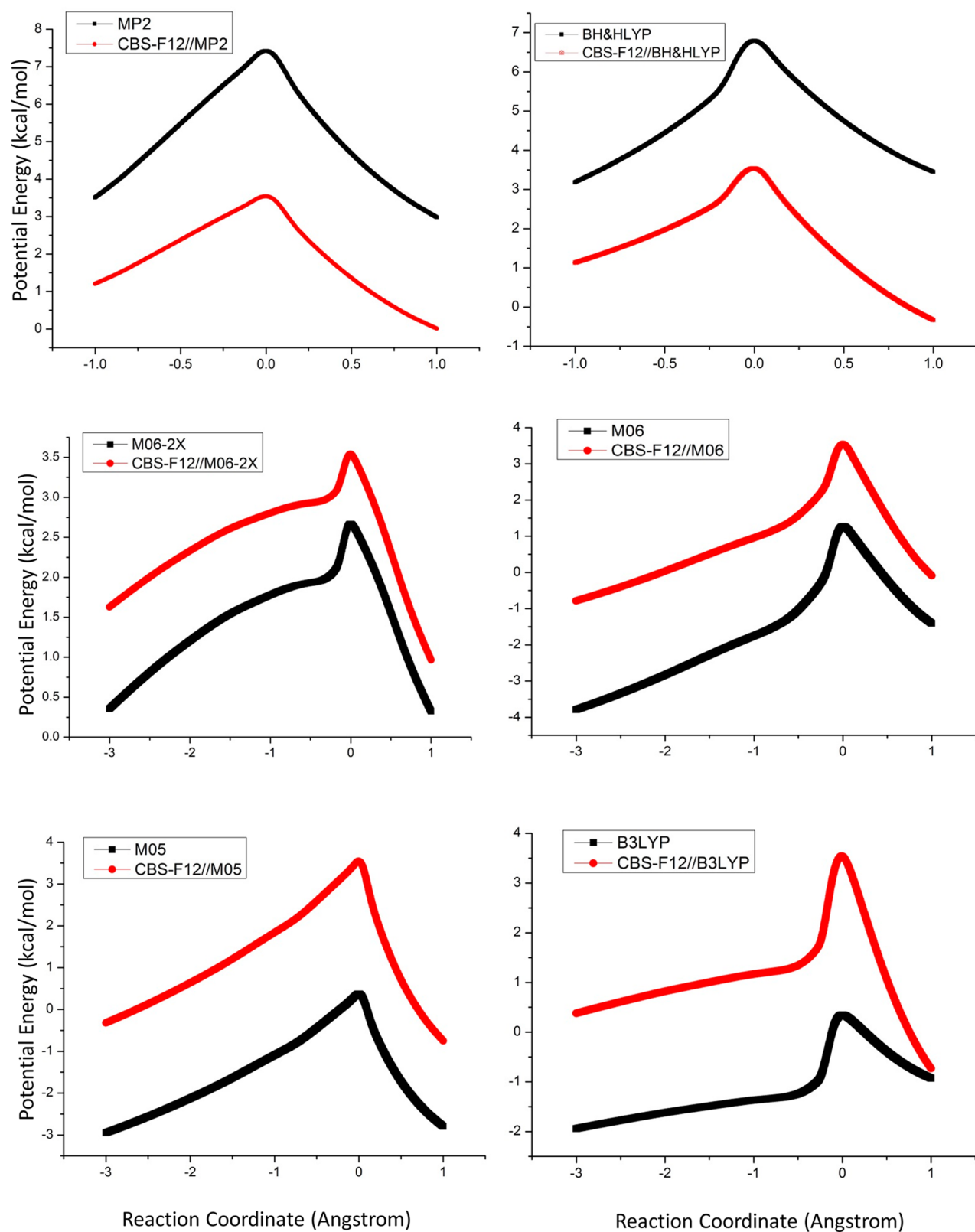
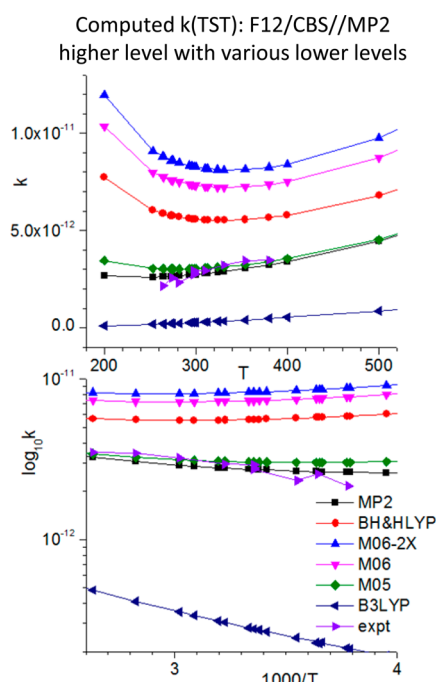


Figure 7. Single- and dual-level VMEP's (see text).

approach, the following criteria have been considered. On the basis of computed energies, although the M06-2X functional gives the best agreement with the ab initio benchmark on  $\Delta E_e^\ddagger$ ,

as discussed above, it does not do so with reaction energy,  $\Delta E_e^{RX}$ . Actually, there is no functional employed here, which performs well on the relative electronic energies for all five



**Figure 8.** Computed  $k^{\text{TST}}$  ( $\text{cm}^3 \text{ molecule}^{-1} \text{ s}^{-1}$ ) versus  $T$  (K) curves (top) and  $\log_{10} k^{\text{TST}}$  versus  $1000/T$  curves (bottom) obtained at different dual levels: F12/CBS//MP2 higher level with different lower levels (experimental values from ref 5).

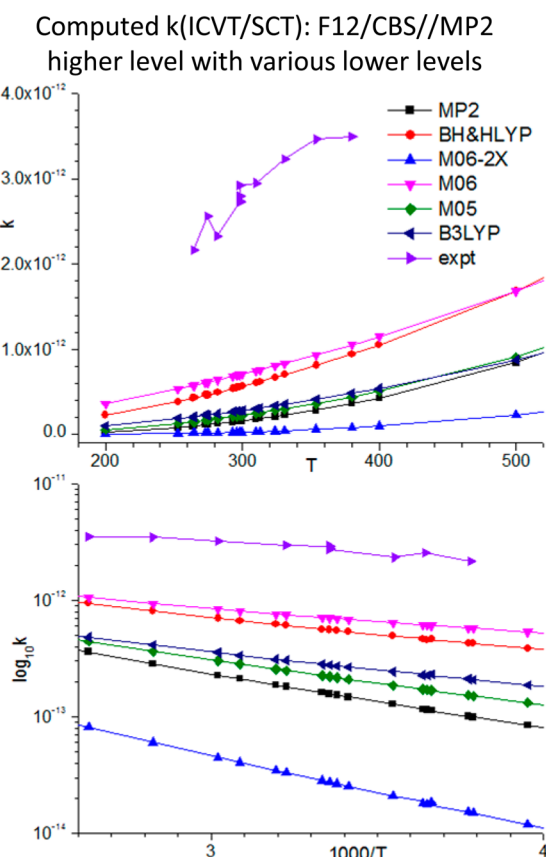


**Figure 9.** Computed  $k^{\text{ICVT/SCT}}$  ( $\text{cm}^3 \text{ molecule}^{-1} \text{ s}^{-1}$ ) versus  $T$  (K) curves (top) and  $\log_{10} k^{\text{ICVT/SCT}}$  versus  $1000/T$  curves (bottom) obtained at different dual levels: F12/CBS//MP2 higher level with different lower levels (experimental values from ref 5).

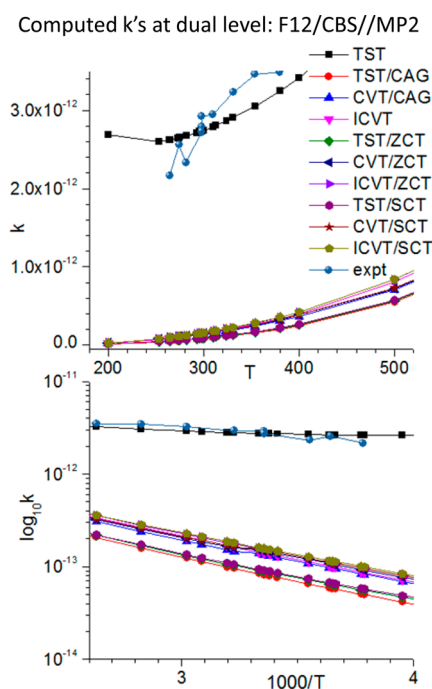


**Figure 10.** Computed  $k$  ( $\text{cm}^3 \text{ molecule}^{-1} \text{ s}^{-1}$ ) versus  $T$  (K) curves (top) and  $\log_{10} k$  versus  $1000/T$  curves (bottom) obtained at various TST levels with the dual level: F12/CBS//MP2 higher level and MP2 lower level (experimental values from ref 5). Because  $k^{\text{CVT}} = k^{\text{ICVT}}$ ,  $k^{\text{CVT}}$  are not plotted (see text).

stationary points considered, as discussed above (see also Table 2). Regarding optimized geometries and computed harmonic vibrational frequencies, the only ab initio method employed is the MP2 method, because analytical first and second derivatives of energy are available with the MP2 method. Higher level ab initio methods {such as the QCISD and CCSD(T) methods} do not have analytical first and/or second derivatives available and hence are impractical for geometry optimization and frequency calculations on the reaction studied. Consequently, no higher ab initio level geometries and vibrational frequencies are available, and it is unsure whether the MP2 results can be considered as benchmarks (see a discussion in ref 1). In summary, it is not obvious which lower level is the best for the purpose, on the basis of the considerations of computed energies, geometries, and vibrational frequencies. Nevertheless, it has been discussed above that geometry effects from different single levels on the computed barrier height are small ( $\sim 0.5 \text{ kcal mol}^{-1}$ ). Lastly, when the effects of using different lower levels on the computed  $k^{\text{ICVT/SCT}}$  values are considered, computed  $k^{\text{ICVT/SCT}}$  values obtained with the MP2 lower level in dual-level calculations are roughly in the middle (in magnitude) of the whole range of computed  $k^{\text{ICVT/SCT}}$  values obtained with all six lower levels (see bottom plots of Figure 9). In view of the above considerations, the MP2 lower level was selected. This also follows the spirit of being as ab initio as possible (i.e., a wavefunction method compared to a DFT method; see ref 1 for a discussion on ab initio versus DFT).

Computed  $k$  versus  $T$  plots with an empirically adjusted barrier of 0.5 or 1.34  $\text{kcal mol}^{-1}$  (without or with Cl spin-orbit corrections, respectively) are shown in Figure 11. It can be seen that computed  $k^{\text{TST}}$  values are too large, whereas computed  $k^{\text{TST/SCT}}$  values (mainly due to  $\kappa^{\text{TST/CAG}}$ , as  $\kappa^{\text{ZCT}} = 1.0$ ) are slightly too small, when compared with experimental values.

Computed  $k$ 's with a fitted barrier height of 0.5 kcal/mol (without spin orbit contribution)

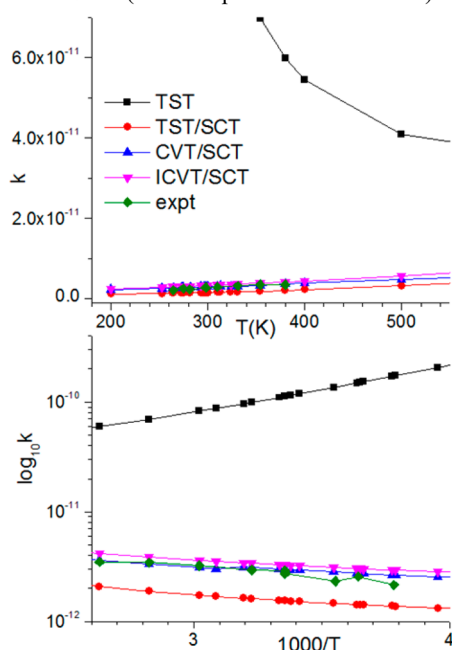


**Figure 11.** Computed  $k$  ( $\text{cm}^3 \text{ molecule}^{-1} \text{ s}^{-1}$ ) versus  $T$  (K) curves (top) and  $\log_{10} k$  versus  $1000/T$  curves (bottom) obtained at various TST levels with the dual level: F12/CBS//MP2 higher level and MP2 lower level, except with a fitted barrier height of 0.5 or 1.34 kcal  $\text{mol}^{-1}$  without and with SO contribution, respectively (experimental values from ref 5). Note that some TST levels are not plotted, because they have the same computed  $k$  values as those plotted, as  $k^{\text{ZCT}} = k^{\text{SCT}} = 1$ ,  $k^{\text{CVT}} = k^{\text{ICVT}}$ , and  $k^{\text{TST/CAG}} = k^{\text{TST/SCT}}$  (see text).

Nevertheless, all other computed  $k$  values, including  $k^{\text{ICVT/SCT}}$  values, agree very well with experimental values. In addition to the magnitude, it is pleasing to see very good agreement in the temperature dependence of  $k$ . The empirically adjusted barrier of 1.34 kcal  $\text{mol}^{-1}$  is 1.16 kcal  $\text{mol}^{-1}$  larger than the experimentally derived activation energy of  $0.71 \pm 0.14$  kcal  $\text{mol}^{-1}$  obtained from the Arrhenius expression of ref 5 and is smaller than the theoretical benchmark value of 3.54 kcal  $\text{mol}^{-1}$  by 2.2 kcal  $\text{mol}^{-1}$ . The uncertainty associated with the computed  $\Delta E_e^\ddagger$  benchmark is  $\pm 0.37$  kcal  $\text{mol}^{-1}$ , based on the difference between the best and F12b/VTZ-F12 values (see footnote *c* of Table 1). If the uncertainty of  $\pm 0.5$  kcal  $\text{mol}^{-1}$  arising from geometry effects (using the B3LYP geometry of the TS in F12 calculations instead of the MP2 geometry), as discussed above, is included, the total uncertainty associated with the theoretical benchmark value is around  $\pm 0.9$  kcal  $\text{mol}^{-1}$ , i.e.,  $3.54 \pm 0.90$  kcal  $\text{mol}^{-1}$  compared to the experimentally derived value of  $0.71 \pm 0.14$  kcal  $\text{mol}^{-1}$  and the empirically fitted value of 1.34 kcal  $\text{mol}^{-1}$ .

Lastly, in the present study, it should be noted that we have only considered one reaction channel, namely the out-of-plane H abstraction of the  $\text{CH}_3\text{-O}$  group, but not abstraction from the in-plane H of the  $\text{CH}_3\text{-O}$  group. A recent computational study on a similar reaction,  $\text{OH} + \text{CH}_3\text{C(O)OCH}_3$ , has considered both channels and concluded from the calculated branching ratios that the out-of-plane H abstraction from the methoxy end is the primary channel at lower temperatures (with computed branching ratios of  $>0.5$  for  $T < 1000$  K, and  $\sim 0.85$  for  $T > 500$  K).<sup>43</sup> In addition, although the computed  $\Delta E_e^\ddagger$  for the out-of-plane H abstraction channel from the

$\text{CH}_3\text{-O}$  group of the  $\text{OH} + \text{CH}_3\text{C(O)OCH}_3$  reaction is 1.66 kcal  $\text{mol}^{-1}$  from ref 43, which is very close to the empirically fitted value of 1.34 kcal  $\text{mol}^{-1}$  for the corresponding  $\text{Cl} + \text{CH}_3\text{C(O)OCH}_3$  reaction considered here, the computed  $\Delta E_e^\ddagger$  for the in-plane H abstraction channel of the  $\text{OH} + \text{CH}_3\text{C(O)OCH}_3$  reaction is 4.90 kcal  $\text{mol}^{-1}$ , 3.24 kcal  $\text{mol}^{-1}$  higher than the out-of-plane H abstraction channel (see ref 43 for details). All these considerations suggest that the out-of-plane H abstraction channel is generally the major channel compared with the in-plane H abstraction channel.

## CONCLUDING REMARKS

We have carried out high level quantum chemical calculations on the reaction path of, and both single- and dual-level direct dynamics rate coefficient calculations at different TST levels on, the  $\text{Cl} + \text{CH}_3\text{C(O)OCH}_3 \rightarrow \text{HCl} + \text{CH}_3\text{C(O)OCH}_2$  reaction. In the investigations on the interrelationship of various levels of theory, the main findings can be summarized as follows:

First, dramatic effects of the changes of the computed harmonic frequency of one vibrational mode along the reaction path on the final computed rate coefficients ( $k$ ) were found. These effects are particularly prominent in a reaction with a low barrier height, as is the case of the reaction studied and can be seen in the large computed CAG correction at the TST level ( $k^{\text{TST/CAG}}$  can be a few orders of magnitude smaller than 1.0 especially at low  $T$ 's). The changes in the computed frequencies from the C–H stretching mode in the reactant, to  $\text{C}\cdots\text{H}\cdots\text{Cl}$  in the TS, and then to H–Cl in the product along the reaction path will be common for all H abstraction reactions by Cl. Nevertheless, including CAG corrections seem to correct for the deficiency in the conventional TST to a large extent. In fact, including the CAG correction at the TST level is similar to the ZK-IRCmax approach in ref 16.

Second, with VTST (CVT or ICVT), it has been found that the maximum of the  $\Delta G$  curve at a certain  $T$  can be at a very negative reaction coordinate ( $-s$ ), particularly when a reaction has a low barrier. This indicates a need for caution, when a VTST calculation is carried out on a reaction with a low barrier, that the range of  $s$  should be wide enough to cover the maximum in the  $\Delta G$  curve. In addition, this could lead to an extreme scenario, when the maximum of the  $\Delta G$  curve actually reaches the reactant complex or the reactants; i.e., no maximum can be located and, hence, VTST is not applicable. Similar situations have also been reported in ref 16 for H abstraction reactions by Cl with low barrier heights.

Third, although the barrier height of a reaction is usually the major factor affecting the computed  $k$ , it has been found that the pre-exponential entropic or partition function term can have significant effects on the computed  $k$  values, particularly when the barrier height is low. From dual-level dynamics calculations of  $k$  employing the same higher level but different lower levels, computed  $k$  values, whether  $k^{\text{TST}}$  or  $k^{\text{ICVT/SCT}}$  values obtained with different lower levels, can have a spread of 1 order of magnitude, which suggests that the uncertainties associated with the computed  $k$  values due to the uncertainties in the lower levels can be also of 1 order of magnitude. This indicates that just improving the reliability of the computed barrier height may not be sufficient to improve computed  $k$  values. In this connection, benchmarking optimized geometries and computed harmonic vibrational frequencies along the reaction path is also important, as concluded previously in ref 1. However, with the size of a reaction system similar to the one studied here, higher level ab initio methods other than the MP2

method, with analytical energy derivatives available, especially second derivatives for computing harmonic vibrational frequencies, are required.

Finally, we have suggested a simple way to obtain higher level IRC paths for mimicking the dual-level direct dynamics approach in calculating  $k$ . We have also obtained computed  $k^{\text{ICVT/SCT}}$  values, which match very well with available experimental values for the  $\text{Cl} + \text{CH}_3\text{C}(\text{O})\text{OCH}_3 \rightarrow \text{HCl} + \text{CH}_3\text{C}(\text{O})\text{OCH}_2$  reaction, by adjusting the barrier height empirically in a dual-level calculation. This empirical barrier of  $1.34 \text{ kcal mol}^{-1}$  is between the theoretical benchmark of  $3.54 \pm 0.90 \text{ kcal mol}^{-1}$  obtained at the UCCSD(T)-F12/CBS//MP/6-311++G\*\* level in the present study and the experimentally derived value of  $0.71 \pm 0.14 \text{ kcal mol}^{-1}$  from ref 5.

## AUTHOR INFORMATION

### Corresponding Authors

\*E. P. F. Lee: e-mail, epl@soton.ac.uk.

\*J. M. Dyke: e-mail, jmdyke@soton.ac.uk.

### Notes

The authors declare no competing financial interest.

## ACKNOWLEDGMENTS

Financial support from the Research Grant Council (RGC) of the Hong Kong Special Administrative Region (HKSAR, Grant Nos. PolyU 5018/09P and 5019/11P), the Research Committee of the Hong Kong Polytechnic University (Account No. A-PK41 and G-YG99) and NERC, UK are acknowledged. The authors are also grateful to the provision of computational resources from the EPSRC (UK) National Service for Computational Chemistry Software. JMD is grateful to the Leverhulme Trust for an Emeritus Fellowship. Very helpful advice from Prof. D. Truhlar and Dr. J. Zheng in the using of POLYRATE is gratefully acknowledged.

## REFERENCES

- (1) Ng, M.; Mok, D. K. W.; Lee, E. P. F.; Dyke, J. M. Rate Coefficients of the  $\text{CF}_3\text{CHFCF}_3 + \text{H} \rightarrow \text{CF}_3\text{CFCF}_3 + \text{H}_2$  Reaction at Different Temperatures Calculated by Transition State Theory with *Ab initio* and DFT Reaction Paths. *J. Comput. Chem.* **2013**, *34*, 545–557.
- (2) Notario, A.; Le Bras, G.; Mellouki, A. Absolute Rate Constants for the Reactions of Cl atoms with a series of Esters. *J. Phys. Chem. A* **1998**, *102*, 3112–3117.
- (3) Christensen, L. K.; Ball, J. C.; Wallington, T. J. Atmospheric Oxidation Mechanism of Methyl Acetate. *J. Phys. Chem. A* **2000**, *104*, 345–351.
- (4) Tyndall, G. S.; Pimentel, A. S.; Orlando, J. J. Temperature Dependence of the Alpha-ester Rearrangement Reaction. *J. Phys. Chem. A* **2004**, *108*, 6850–6856.
- (5) Cuevas, C. A.; Notariob, A.; Martineza, E.; Albaladejo, J. Influence of Temperature in the Kinetics of the Gas-phase Reactions of a series of Acetates with Cl atoms. *Atmos. Environ.* **2005**, *39*, 5091–5099.
- (6) Andersen, V. F.; Nilsson, E. J. K.; Jørgensen, S.; Nielsen, O. J.; Johnson, M. S. Methyl Acetate Reaction with OH and Cl: Reaction Rates and Products for a Biodiesel Analogue. *Chem. Phys. Lett.* **2009**, *472*, 23–29.
- (7) Schutze, N.; Zhong, X.; Kirschbaum, S.; Bejan, I.; Barnes, I.; Benter, T. Relative Kinetic Measurements of Rate Coefficients for the Gas-phase Reactions of Cl atoms and OH radicals with a series of Methyl Alkyl Esters. *Atmos. Environ.* **2010**, *44*, 5407–5414.
- (8) Middala, S.; Campell, S.; Olea, C.; Scruggs, A.; Hasson, A. S. Kinetics and Mechanism of the Reaction of Propylene Oxide with Chlorine Atoms and Hydroxy Radicals. *Int. J. Chem. Kinet.* **2011**, *43*, 507–521.
- (9) Poutsma, M. L. Evolution of Structure-Reactivity Correlations for the Hydrogen Abstraction Reaction by Chlorine Atom. *J. Phys. Chem. A* **2013**, *117*, 687–703.
- (10) Finlayson-Pitts, B. J. Halogens in the Troposphere. *Anal. Chem.* **2010**, *82*, 770–776.
- (11) Finlayson-Pitts, B.; Pitts, J. R. *Chemistry of the Upper and Lower Atmosphere*; Academic Press: San Diego, CA, 2000.
- (12) Raff, J. D.; Njagic, B.; Chang, W. L.; Gordon, M. S.; Dabdub, D.; Gerber, B.; Finlayson-Pitts, B. J. Chlorine Activation Indoors and Outdoors via Surface-mediated Reactions of Nitrogen Oxides with Hydrogen Chloride. *Proc. Natl. Acad. Sci. U. S. A.* **2009**, *106*, 13647–13654.
- (13) De Haan, D. O.; Brauers, T.; Oum, K.; Stutz, J.; Nordmeyer, T.; Finlayson-Pitts, B. Heterogeneous Chemistry in the Troposphere: Experimental Approaches and Applications to the Chemistry of Sea Salt Particles. *J. Int. Rev. Phys. Chem.* **1999**, *18*, 343–385.
- (14) Pszenny, A. A. P.; Moldanov, J.; Keene, W. C.; Sander, R.; Maben, J. R.; Martinez, M.; Crutzen, P. J.; Perner, D.; Prinn, R. G. Halogen Cycling and Aerosol pH in the Hawaiian Marine Boundary Layer. *Atmos. Chem. Phys.* **2004**, *4*, 147–168.
- (15) Wayne, R. P. *Chemistry of Atmospheres*, 3rd ed.; Oxford University Press: Oxford, U.K., 2000.
- (16) Chan, B.; Radom, L. Approaches for Obtaining Accurate Rate Constants for Hydrogen Abstraction by a Chlorine Atom. *J. Phys. Chem. A* **2012**, *116*, 3745–3752.
- (17) Frisch, M. J.; Trucks, G. W.; Schlegel, H. B.; Scuseria, G. E.; Robb, M. A.; Cheeseman, J. R.; Scalmani, G.; Barone, V.; Mennucci, B.; Petersson, G. A.; et al. *Gaussian 09*, revision A.02; Gaussian, Inc.: Wallingford, CT, 2009.
- (18) Adler, T. B.; Knizia, G.; Werner, H. J. A Simple and Efficient CCSD(T)-F12 Approximation. *J. Chem. Phys.* **2007**, *127*, 221106.
- (19) Werner, H.-J.; Knowles, P. J.; Knizia, G.; Manby, F. R.; Schütz, M. Molpro: a General-Purpose Quantum Chemistry Program Package. *WIREs Comput. Mol. Sci.* **2012**, *2*, 242–253.
- (20) Werner, H.-J.; Knowles, P. J.; Knizia, G.; Manby, F. R.; Schütz, M.; et al. MOLPRO, version 2010.1, see <http://www.molpro.net>.
- (21) Helgaker, T.; Klopper, W.; Tew, D. P. Quantitative Quantum Chemistry. *Mol. Phys.* **2008**, *106*, 2107–2143.
- (22) Peterson, K. A.; Adler, T. B.; Werner, H.-J. Optimized Auxiliary Basis Sets for Explicitly Correlated Methods. *J. Chem. Phys.* **2008**, *128*, 084102.
- (23) Hill, J. G.; Mazumder, S.; Peterson, K. A. Correlation Consistent Basis Sets for Molecular Core-valence Effects with Explicitly Correlated Wavefunctions: The Atoms B-Ne and Al-Ar. *J. Chem. Phys.* **2010**, *132*, 054108.
- (24) Weigend, F.; Köhn, A.; Hättig, C. Efficient Use of the Correlation Consistent Basis Sets in Resolution of the Identity MP2 Calculations. *J. Chem. Phys.* **2002**, *116*, 3175–3183.
- (25) Knizia, G.; Adler, T. B.; Werner, H.-J. Local Explicitly Correlated Second-order Perturbation Theory for the Accurate Treatment of Large Molecules. *J. Chem. Phys.* **2009**, *130*, 054104.
- (26) Helgaker, T.; Klopper, W.; Koch, H.; Noga, J. Basis-set Convergence of Correlated Calculations on Water. *J. Chem. Phys.* **1997**, *106*, 9639–9646.
- (27) Halkier, A.; Helgaker, T.; Klopper, W.; Jørgensen, P.; Csaszar, A. G. Comment on “Geometry Optimization with an Infinite Basis Set” [*J. Phys. Chem. A* 1999, *103*, 651] and “Basis-set Extrapolation” [*Chem. Phys. Lett.* 1998, *294*, 45]. *Chem. Phys. Lett.* **1999**, *310*, 385–389.
- (28) Zheng, J.; Zhang, S.; Lynch, B. J.; Corchado, J. C.; Chuang, Y.-Y.; Fast, P. L.; Hu, W.-P.; Liu, Y.-P.; Lynch, G. C.; Nguyen, K. A. et al. POLYRATE version 2010-A (June, 2010), Copyright 1988–2010 D. G. Truhlar and Regents of the University of Minnesota, Minneapolis, MN, U.S.A.
- (29) Hratchian, H. P.; Schlegel, H. B. Using Hessian Updating to Increase the Efficiency of a Hessian based Predictor-corrector Reaction Path following Method. *J. Chem. Theory Comput.* **2005**, *1*, 61–69.



- (30) Hratchian, H. P.; Schlegel, H. B. Accurate Reaction Paths Using a Hessian based Predictor-corrector Integrator. *J. Chem. Phys.* **2004**, *120*, 9918–9924.
- (31) Wigner, E. P. The Transition State Method. *Trans. Faraday Soc.* **1938**, *34*, 29–41.
- (32) Fernández-Ramos, A.; Miller, J. A.; Klippenstein, S. J.; Truhlar, D. G. Modeling the Kinetics of Bimolecular Reactions. *Chem. Rev.* **2006**, *106*, 4518–4584.
- (33) Radziemski, L. J., Jr.; Kaufman, V. Wavelengths, Energy Levels and Analysis of Neutral Atomic Chlorine (Cl I). *J. Opt. Soc. Am.* **1969**, *59*, 424–443.
- (34) Chuang, Y.-Y.; Truhlar, D. G. Statistical Thermodynamics of Bond Torsional Modes. *J. Chem. Phys.* **2000**, *112*, 1221–1228; Erratum *J. Chem. Phys.* **2004**, *121*, 7036.
- (35) Ellingson, B. A.; Lynch, V. A.; Mielke, S. L.; Truhlar, D. G. Statistical Thermodynamics of Bond Torsional Modes: Tests of Separable, Almost-separable, and Improved Pitzer-Gwinn Approximations. *J. Chem. Phys.* **2006**, *125*, 084305.
- (36) Donahue, N. M.; Anderson, J. G.; Demerjian, K. L. New Rate Constants for Ten OH Alkane Reactions from 300 to 400 K: An Assessment of Accuracy. *J. Phys. Chem. A* **1998**, *102*, 3121–3126.
- (37) IUPAC. *Compendium of Chemical Terminology*, 2nd ed. (the “Gold Book”); Compiled by A. D. McNaught and A. Wilkinson. Blackwell Scientific Publications, Oxford, U.K., 1997. XML on-line corrected version: <http://goldbook.iupac.org> (2006–) created by M. Nic, J. Jirat, and B. Kosata; updates compiled by A. Jenkins. ISBN 0-9678550-9-8. DOI: 10.1351/goldbook.
- (38) Hamborg, E. S.; Versteeg, G. F. Absorption and Desorption Mass Transfer rates in Chemically Enhanced Reactive Systems. Part II: Reverse Kinetic Rate Parameters. *Chem. Eng. J.* **2012**, *198*–199, 561–570.
- (39) Aquilanti, V.; Mundim, K. C.; Cavalli, S.; De Fazio, D.; Aguilar, A.; Lucas, J. M. Exact Activation Energies and Phenomenological Description of Quantum Tunneling for Model Potential Energy Surfaces. The F + H<sub>2</sub> Reaction at Low Temperature. *Chem. Phys.* **2012**, *398*, 186–191.
- (40) Linstrom, P. J.; Mallard, W. G., Eds. *NIST Chemistry WebBook*; NIST Standard Reference Database Number 69; National Institute of Standards and Technology: Gaithersburg, MD, <http://webbook.nist.gov> (retrieved September 18, 2013).
- (41) Cox, J. D.; Wagman, D. D.; Medvedev, V. A. *CODATA Key Values for Thermodynamics*; Hemisphere Publishing Corp.: New York, 1984; p 1.
- (42) Hall, H. K., Jr.; Baldt, J. H. Thermochemistry of Strained-Ring Bridgehead Nitriles and Esters. *J. Am. Chem. Soc.* **1971**, *93*, 140–&.
- (43) Yang, L.; Liu, J.-y.; Li, Z.-s. Theoretical Studies of the Reaction of Hydroxyl Radical with Methyl Acetate. *J. Phys. Chem. A* **2008**, *112*, 6364–6372.
- (44) Senent, M. L.; Domínguez-Gómez, R.; Carvajal, M.; Kleiner, I. Highly Correlated *Ab initio* Study of the Far Infrared Spectra of Methyl Acetate. *J. Chem. Phys.* **2013**, *138*, 044319.
- (45) Tudorie, M.; Kleiner, I.; Hougen, J. T.; Melandri, S.; Sutikdja, L. W.; Stahl, W. A fitting program for Molecules with Two Inequivalent Methyl Tops and a Plane of Symmetry at Equilibrium: Application to New Microwave and Millimeter-wave Measurements of Methyl Acetate. *J. Mol. Spectrosc.* **2011**, *269*, 211–225.
- (46) Fernandez-Ramos, A.; Ellingson, B. A.; Garret, B. C.; Truhlar, D. G. In *Reviews in Computational Chemistry*; Lipkowitz, K. B., Cundari, T. R., Eds.; Wiley-VCH: Hoboken, NJ, 2007; Vol. 23, pp 125.

## ■ NOTE ADDED IN PROOF

A search has been made for the TS for the in-plane H-abstraction for the Cl + CH<sub>3</sub>C(O)OCH<sub>3</sub> → HCl + CH<sub>3</sub>C(O)OCH<sub>2</sub> reaction using the M06-2X functional. The TS was found to be the same as that for the out-of-plane H-abstraction. This is because the product CH<sub>3</sub>C(O)OCH<sub>2</sub> has the CH<sub>2</sub> moved to an in-plane position, after a H has been abstracted from the –OCH<sub>3</sub> group. A notable difference

between the Cl and OH reactions with CH<sub>3</sub>C(O)OCH<sub>3</sub> is that with OH, hydrogen bonding between the H atom of the O–H group and the O atom of the –OCH<sub>3</sub> group (forming a planar five-membered ring in the TS) which would stabilise an “in-plane” TS structure (the TS1b structure in Figure 1 of ref 43) is possible; this is not possible in the Cl case.